WILEY-VCH

Femtosecond Laser-Written Invisible Sensors in Architectural Glass and their Impact on Strength

Shahryar Nategh [a,b], Viktor Geudens [a], Geert Van Steenberge [a], Jan Belis [b,+], Jeroen Missinne [a,+,*]

[a] Centre for Microsystems Technology (CMST), imec and Ghent University, Technologiepark-Zwijnaarde 126, 9052, Belgium

[b] Magnel-Vandepitte Laboratory, Department of Structural Engineering and Building Materials, Ghent University, Technologiepark-Zwijnaarde 60, 9052, Belgium

[+] Contributed equally as last author

[*] Corresponding author, Jeroen.Missinne@UGent.be

Keywords

Architectural glass, Bragg grating, femtosecond laser, strength, waveguide.

Abstract

Monitoring architectural glass is becoming increasingly important due to its transition from small infill panels to large, load-bearing applications, but traditional sensors are visually unappealing for use with transparent materials. This study explores the integration of waveguide Bragg gratings (WBG) into 4 mm thick soda lime silicate architectural glass using femtosecond laser technology, creating invisible optical sensors within the bulk. This method furthermore protects the sensors from surface damage. We report on the optimization and characterization of laser-written waveguides in this type of glass, achieving low-loss single-mode waveguides up to 25 cm long with a propagation loss of 0.52 dB cm^{-1} at 1550 nm wavelength. Furthermore, WBGs are realized showing a 12.8% peak reflectivity and 115 pm−3 dB bandwidth. A demonstrator consisting of a 25 cm-long architectural glass plate with a WBG in the center connected to the edge via a single-mode waveguide, shows a strain sensitivity of 1.20 pm $\mu\varepsilon^{-1}$ and a temperature sensitivity of 13.5 pm °C^{-1}. Importantly, mechanical testing confirms that the waveguides do not compromise the strength of the glass which is crucial when subjected to loads. These findings underscore the potential of this technology for structural health monitoring of glass structures.

.

S. Nategh, V. Geudens, G. Van Steenberge, J. Belis, J. Missinne, Femtosecond Laser-Written Invisible .
Sensors in Architectural Glass and Their Impact on Strength. Adv. Mater. Technol. 2025, 2401941. https://doi.org/10.1002/admt.202401941

1. Introduction

In the past, glass in buildings was mainly used as an infill material, primarily in smaller panels and windows. However, with the increasing size of glass elements and their expanded use in large glass facades, loads on the glass have become more pronounced and determining [1]. Modern applications now rely more heavily on the strength of the glass, which is directly linked to the various loads it must withstand, such as wind, snow, earthquakes, floor loads, explosions, fire, vehicle impacts and temperature effects [2]. This necessitates a new approach to design and maintain these structures [3]. For other structural materials such as concrete, steel or composites, sensors are nowadays commonly being used for structural health monitoring (SHM) offering huge benefits for accurate service or lifetime prediction. However, there is currently no acceptable sensing technology that would allow a widespread implementation of SHM on glass structures. The reason is that current sensing solutions for SHM such as strain gages [4], accelerometers [5], thermocouples [6], and Fiber Bragg Grating (FBG) sensors [7] would need to be attached to the surface, which would appear as visually unappealing thereby jeopardizing the transparency and architectural integrity of the glass structures.

Focused femtosecond lasers, however, can be used to locally modify the glass properties by non-linear absorption. These modifications in the focal volume of the laser light results in modification of the refractive index on the micrometer scale [8]. This localized modification is used to realize high-quality optical structures such as waveguides [9] and sensors [10] directly in the bulk of the glass by translating the focal volume through the glass substrate, easily allowing fabrication of 3D structures [11]. The single step laser direct writing of complex optical circuits enables fast fabrication times and flexibility in design, making this an interesting technology for both fast prototyping as well as industrial production. Realizing such sensors at a certain depth renders them invisible and furthermore protects them from harsh operating conditions. Femtosecond laser written sensors therefore seem to have great potential for applications in architectural glass but have until now not found their way into the market for multiple reasons. Firstly, work reported on femtosecond laser inscription until now has focused on several types of high-grade technical glass [12], mostly used in electronics, semiconductor or other precision applications, such as fused silica [13], borosilicate [14], phosphate [15], chalcogenide [16], and various doped glass substrates [17], although in architectural applications a lower grade type of soda lime silicate (SLS) glass is used which is more affordable because of its relatively low melting point and relaxed requirements in terms of number of impurities or defects and thickness uniformity. Some data, although very limited, has been published on femtosecond laser inscription in SLS glass [17a, 18], however reported publications were using technical grade (e.g. extra white SLS) glass. Secondly, the scale of glass used in architectural applications is much larger. While work until now has focused on realizing relatively short (in the order of centimeters) structures in technical glass which is furthermore relatively thin (<1 mm), architectural glass is thicker, ranging from 2 mm to 25 mm, and sizes of tens of centimeters up to meters are common [19]. Thirdly, the inscribed structures are essentially local defects which may potentially jeopardize the mechanical strength of the glass, which obviously needs to be studied for architectural applications. The strength of the glass, especially when used in load-bearing applications such as windows or panels, must be meticulously evaluated to prevent potential failures [20]. Generally, glass strength is affected by natural surface flaws that develop during production, transportation, and usage [19]. Many studies have been conducted regarding the effects of surface flaws on the strength of architectural glass [21]. However, there has been a paucity of studies investigating the influence of bulk modifications on glass strength [22], particularly in SLS architectural glass. The primary reason for the lack of publications on this topics is that in SLS architectural glass, surface flaws arising from production, transport, handling, or cleaning are the dominant factors affecting strength, while bulk defects such as bubbles are rare which have thus until now considered negligible [19, 23].

With the current work, we want to close these research gaps by investigating in detail the femtosecond laser modification of SLS glass used in architectural applications with the aim to realize sensors and interconnecting waveguides using optimized laser parameters. We furthermore realized demonstrator structures at a scale (25 cm) that allows reliable mechanical testing using standardized methods proving functionality of the sensors as well as studying their impact on the mechanical strength of the glass. Waveguide Bragg grating (WBG) sensors, a planar implementation of fiber Bragg gratings [24], were chosen due to their proven reliability and numerous advantages, including electrically passive operation, immunity to electromagnetic interference (EMI), high sensitivity, and multiplexing capabilities [25]. These sensors are already widely used commercially for structural health monitoring (SHM), such as strain and temperature sensing, and their realization using femtosecond laser technology has been demonstrated in other types of glass [26]. The demonstrator structure featured in this work consisted of a WBG realized in a 25 cm long piece of architectural SLS glass. The WBG was realized by periodically modifying the refractive index along a 10 mm section in the center of the glass, using fs laser inscription, and was interconnected to the glass edge with a single mode waveguide, also realized using fs laser inscription. Since WBGs operate as wavelength-selective mirrors, they can conveniently be read out in reflection using only a single fiber connected to the edge of the glass. This configuration allowed for the demonstration of strain and temperature sensing in architectural SLS glass, while maintaining the transparency and architectural aesthetics of the material. Furthermore, it proved that the laser-inscribed sensing structures did not compromise the mechanical strength of the glass. These findings underline the potential of femtosecond laser technology to enable structural health monitoring in glass structures without affecting their functionality or visual appeal.

2. Results and discussion

2.1. Femtosecond laser-written waveguides in SLS glass

Waveguides and Bragg gratings have been realized into the bulk of architectural SLS glass using a two-step inscription method employing a femtosecond laser (Figure 1a). Firstly, the effect of pulse energy (200 nJ to 600 nJ), translation speed (0.05 mm/s to 20 mm/s) and writing depth (50 µm and 100 µm below the surface) on the laser-modified zone (LMZ) and on the resulting waveguide properties was investigated in detail. The fs laser polarization (parallel to the writing direction) was kept fixed since changing the polarization did not affect the results noticeably.

Figure 1b illustrates with cross-sectional images how pulse energy and writing speed affect the LMZ in the bulk of the glass (for a 500 kHz laser frequency and a writing depth of 100 µm). As expected, the LMZ increases with increasing pulse energy and decreasing writing speed. The cross-sectional images also clearly reveal the inner plasma zone (IPZ) and heat affected zone (HAZ) [27] showing that, for the studied laser conditions, the mechanism of bulk modification in SLS glass relies on the thermal accumulation effect as also reported for modification of borosilicate glass at high pulse frequencies [28]. The rapid resolidification after the laser exposure causes a local refractive index change which, when optimized properly, can result in low-loss single mode waveguides. It has been reported that light propagation occurs in a sub-region of the inner plasma zone (IPZ) characterized by a local positive increase in refractive index and discernible as a small white spot under optical transmission microscopy (Figure S1, Supporting information) [28c, 29].

Figure 1c shows the total insertion loss for 20 mm long waveguides interfaced with single mode fibers from both sides and measured at 1550 nm wavelength, for a selection of combinations of pulse energy and writing speed, with a fixed frequency of 500 kHz and a writing depth of 100 µm. Data corresponding to other laser parameters can be found in Figure S2 (Supporting Information). The graph indicates that low insertion losses are achieved for a combination of (350 nJ and 0.5 mm/s) and (550 nJ and 0.1 mm/s) pulse energy and writing speed, respectively. However, this overall insertion loss includes both fiber-to-waveguide coupling losses and the waveguide propagation losses. Therefore, to estimate the coupling losses which are caused by mode mismatch, waveguide near-field mode profiles (1550 nm wavelength) were measured for sets of laser parameters yielding low overall insertion loss, as shown in Figure 1d along with respective cross-sectional images. Although all plotted mode profiles look similar and insertion losses are comparable, undesirable multimode behavior and multiple guiding regions were observed for waveguides written at 550 nJ and 0.1 mm/s due to the larger LMZ [30]. The multiple guiding regions are a result of the combination of high pulse energy and low writing speed as visualized by recorded mode profiles shown in Figure S3 (Supporting Information). For waveguides written at 350 nJ and 0.5 mm/s, changing the incoupling conditions (specifically, the lateral position of the optical fiber relative to the waveguide's input facet) did not affect the mode profile indicating these waveguides are single mode and the measured mode field diameter (MFD) of 16.2 µm in the x-direction (MFDx) and 14.4 µm in the y-direction (MFDy) indicate a good coupling efficiency with SMF-28 single mode fibers (MFD 10.4 ± 0.5 µm) is possible. The cut-back measurement (cfr. Figure 2a) performed for waveguides (n = 10) written with these parameters allowed quantifying their coupling loss (i.e. 1.49 ± 0.14 dB) and propagation loss (i.e. 0.52 ± 0.01 dB/cm) reliably. Note that a systematic cut-back was performed starting from a 14 cm long sample that was progressively shortened in steps of approximately 1 cm (exact length was plotted), while we also added the datapoint corresponding to a separate sample with 25 cm-long waveguides (n = 10) being the length of the demonstrator discussed below. To the best of our knowledge, this is amongst the longest straight femtosecond laser-written waveguides that has been reported and characterized in planar glass. Furthermore, the low standard deviation of the results suggests a high degree of uniformity in the fabricated waveguides.

The waveguides did not show a measurable polarization dependent waveguide loss, likely due to the formation process involving melting and resolidification of the glass yielding sufficiently low-stress circular waveguides, consistent with findings for waveguides realized in other types of glass also relying on the thermal accumulation mechanism [18b, 31]. Typically, high birefringence is observed due to non-circular waveguide geometry or asymmetric stress produced during the laser inscription process which could result in nanogratings formed within the laser-modified volume, commonly observed in fused silica glass [28c, 32]. In borosilicate glass, which has a glass transition temperature closer to that of SLS glass [33], nanogratings have not been observed when heat accumulation takes place [34].

The low propagation loss of 0.52 dB/cm at a wavelength of 1550 nm is comparable to the lowest waveguide loss reported at 1550 nm (0.5 dB/cm) for technical grade SLS glass (Corning 0215) [18b], and it is lower than the lowest waveguide loss reported at 800 nm (0.86 dB/cm) for extra-white SLS glass [18c]. It should also be noted that, although these technical glasses are generally classified as SLS, they have a slightly different composition compared to the standard SLS glass commonly used in the construction sector (see Table S2, Supporting Information), which is used in this work. Additionally, our results are slightly higher than the low propagation loss of approximately 0.3 dB/cm reported for technical grade borosilicate glass (Corning EAGLE2000) at 1550 nm [28c] and the recently achieved low propagation loss in borosilicate glass Corning Eagle XG, which span from approximately 0.1 dB/cm to 0.2 dB/cm at 1550 nm [35]. Considering the recent trend of using thin, aluminosilicate chemically strengthened glass for architectural applications [36], there may be opportunities to further reduce losses by using such materials [37]. Despite using architectural grade glass, the obtained loss values are close to those of waveguides realized in technical grade glass. This may be attributed to the waveguide formation process based on the heat accumulation mechanism, which causes local melting and resolidification. This process may have been quite tolerant to the larger amount of impurities and inhomogeneities typically found in architectural glass, potentially mitigating them and resulting in high-quality waveguides in this type of glass.

Figure 2b plots the total insertion loss for a 2 cm-long waveguide (350 nJ and 0.5 mm/s) as a function of wavelength within the typical range used by Bragg grating sensors, showing a minimum around 1560 nm with a broad 1 dB bandwidth of 50 nm. Since the material loss does not significantly differ in the studied wavelength range [38], the slight wavelength dependence observed in the insertion loss, is propagation loss and coupling loss. The propagation loss is dominated by a Rayleigh scattering contribution (C/λ^4), which is believed to be caused by sub-wavelength inhomogeneities in the refractive index modification, explaining the increasing loss for shorter wavelengths [13c, 39]. The coupling loss is influenced by the MFD of the waveguide and its mismatch with the fiber. This MFD can increase significantly when the waveguides operate near the cut-off condition at longer wavelengths, which may explain the increased loss at these wavelengths.

Although a waveguide writing depth of 50 μm was also investigated, several factors justify the choice for a 100 μm writing depth as a suitable compromise. Firstly, the insertion loss for waveguides written 50 μm deep is generally higher than for waveguides written 100 μm deep (see Figure S4 in Supporting Information). This is attributed to the decreased pulse energy threshold for the formation of waveguides and ablation occurring at lower pulse energies when focusing closer to the surface [40]. This results in a more limited parameter space and generally weaker index change for waveguides written close to the surface [40b]. Secondly, having the waveguides deeper in the glass protects them from natural surface flaws, which can be tens of micrometers deep [41]. On the other hand, increasing the depth too drastically can reduce the eventual sensor's strain sensitivity to bending (cfr. Figure S5, Supporting information).

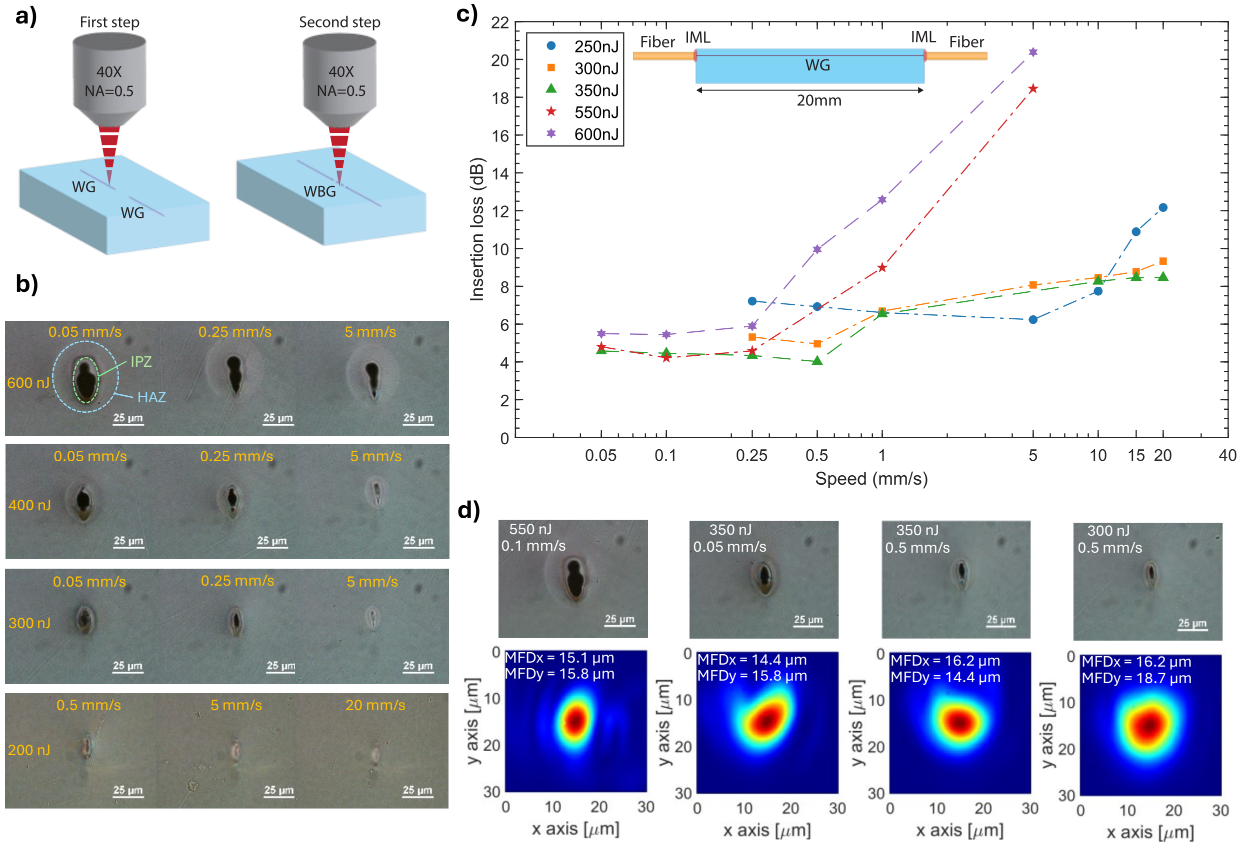

Figure 1. a) Schematic illustrating the two-step process of inscribing waveguides (WG) and Waveguide Bragg Gratings (WBG) in the bulk of the glass. b) Microscopic cross-sectional images (diascopic illumination) illustrating the LMZ for various laser pulse energies and writing speeds. c) Total insertion loss for 20mm long waveguides as a function of writing speed and pulse energy (n = 10). The schematic illustrates the loss measurement configuration, including the glass WG sample, single mode fibers, and index matching liquid (IML). d) Microscopic cross-sectional images (diascopic illumination) and corresponding waveguide mode profiles for selected laser parameters.

2.2. Femtosecond laser-written Bragg grating sensors in SLS glass

Waveguide Bragg gratings were realized by modulating the fs laser pulse train with an acousto-optic modulator while inscribing [42]. According to the Bragg equation ($\lambda_B = 2n_{eff}\Lambda$), where λ_B is the Bragg wavelength, n_{eff} is the effective refractive index, and Λ is the grating period, the modulation frequency (981 Hz) in combination with the writing speed (0.5 mm/s) was chosen to obtain the desired grating period ($\Lambda = 0.510$ µm) to achieve a Bragg wavelength (λ_B) in the 1520 - 1580 nm range to be compatible with commercial interrogators. The optimal laser parameters for realizing WBG in architectural SLS glass were determined by studying the effect of pulse energy (200 nJ to 600 nJ), writing speed (0.05 mm/s to 10 mm/s), duty cycle (10% to 90%) and grating length (1 mm to 20 mm) on the reflection spectrum. The laser frequency was kept fixed at 500 kHz, the polarization was kept parallel to the writing direction and the depth was maintained at 100 µm similarly as for the laser-written waveguides as discussed above. The highest reflectivity was achieved using a pulse energy of 250 nJ, a writing speed of 0.5 mm/s, and a duty cycle of 50%. Figure 2c shows the microscopic cross-section and measured near-field profile with MFDx = 19.4 μm and MFDy = 21.5 μm, corresponding to these laser parameters. The larger MFD of the Bragg grating waveguide compared to that of the standard waveguide will result in coupling loss when transitioning from the standard waveguide to the Bragg grating waveguide.

Figure 2d shows the effect of the duty cycle on the reflection spectrum of 10 mm long Bragg gratings while data illustrating the effect of other laser parameters can be found in Figures S6 and S7 (Supporting Information). The figure shows that a 12.8% peak reflectivity (-3 dB bandwidth: 115 pm) is obtained for 50% duty cycle which at the selected modulation frequency (981 Hz) corresponds with 510 laser pulses per period or 255 laser pulses per burst. Too low duty cycles cause too little modification (e.g. 25 pulses per burst region at 10 % duty cycle) limiting the refractive index contrast, while too high duty cycles (e.g. 459 pulses per burst region at 90% duty cycle) do not allow sufficient cooling between bursts and result in overlap of the LMZs of consecutive burst regions [43]. This thermal effect may blur the grating lines, reducing the precision of the periodic structure and potentially decreasing reflectivity [44]. Thus, as seen in Figure 2d, reflectivity increases rapidly from a 10% to 50% duty cycle because of increasing index contrast. Beyond 50% duty cycle, reflectivity reduces, likely because of reducing index contrast due to excessive overlap of the LMZs between the different periods. Comparing to fused silica glass, where Bragg gratings are written outside the cumulative heating regime, typically higher reflectivity can be obtained (>90%) and the effect of duty cycle is more gradual [42, 45].

Figure 2e shows the influence of the Bragg grating length on the reflection spectrum for the selected laser parameters, indicating a gradual increase in peak reflectivity with increasing length up to a measured 20.8 % for 20 mm, which is as expected since longer gratings exhibit more interaction with the light, which leads to more partial reflection at each interface until all light at the Bragg wavelength is reflected [46]. Note that these plots include two times the coupling loss (approximately 3 dB in total, cfr. Figure 2a) meaning that the pure grating reflectivity is about double the plotted value. While longer Bragg gratings result in a higher reflectivity, they reduce the spatial resolution of the eventual sensors. Typically, longer gratings also result in a lower 3-dB bandwidth, making the peak more sharp and well-defined [47]. However, this requires a perfect fabrication method, since slight differences during fabrication in for example translation speed, will lead to non-uniform grating and a distortion of the resonance peak [48]. Additionally, the insertion loss of waveguide Bragg gratings was measured to be approximately twice that of the optimized waveguides, indicating that increasing the grating length also introduces additional loss for possible future multiplexed gratings. This leads to a decreasing reflectivity for each following Bragg grating [48]. Finally, in the field of sensing, long gratings can be a drawback, especially when non-uniform changes are applied to the sensor. A temperature or strain gradient will affect different parts of the WBG to a different amount, leading to a distortion of the sensor response. As longer WBGs are more exposed to the non-uniform change, they are more prone to this unwanted behaviour, compared to shorter grating lengths which can be used for higher gradients [49]. Therefore a grating length of 10 mm was chosen for realizing the eventual demonstrator which consisted of a Bragg grating with interconnecting waveguide sections (cfr. Figure 1a and Figure 4a). Since different laser parameters used to create the Bragg grating and the waveguide section result in different LMZs, the influence of the waveguide-to-grating section alignment (in the depth and transversal direction) was investigated (cfr. Figure S8, Supporting Information). These tests confirmed that the highest overall reflectivity is achieved when the laser is focused at the same depth without offset in the lateral direction for the consecutive sections.

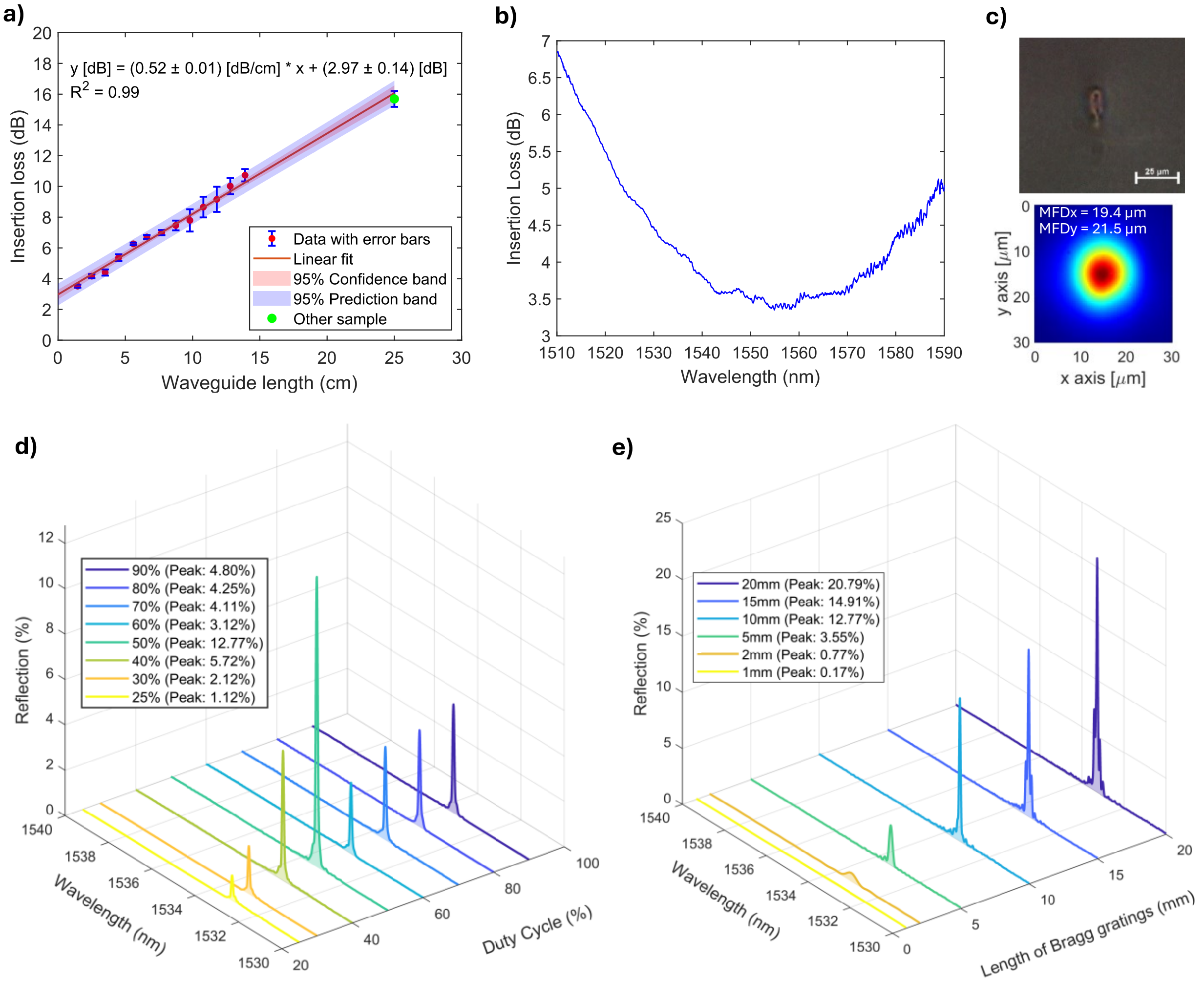

Figure 2. a) Insertion loss as a function of waveguide length realized with the optimal laser parameters (pulse energy 350 nJ, writing speed 0.5 mm/s) resulting from cut-back measurements (n = 10). The result for a 25 cm length, indicated by the green marker, was obtained using a different sample (n = 10). b) Insertion loss of a 20 mm long waveguide section (pulse energy 350 nJ, writing speed 0.5 mm/s) as a function of wavelength. c) Microscopic cross-section (diascopic illumination) and near-field mode profiles corresponding to a waveguide Bragg grating section (pulse energy 250 nJ, speed 0.5 mm/s, duty cycle 50%). d) Influence of the duty cycle of the modulated pulse train on the reflection spectrum of a 10 mm long waveguide Bragg grating (pulse energy 250 nJ, speed 0.5 mm/s). e) Influence of the Bragg grating length on the reflection spectrum of waveguide Bragg gratings (pulse energy 250 nJ, speed 0.5 mm/s, duty cycle 50%). Plotted reflection values include a coupling loss of approximately 3 dB.

2.3. Laser-modified glass strength

Since surface [21a, 21b, 50] and bulk [22] defects are known to influence glass strength, it is important to study the strength effect of bulk laser modification when aiming at structural applications. To evaluate the bending strength of glass, four-point bending tests (Figure 3a) were conducted on two groups of thirty samples each (nominal dimensions 25 cm x 4 cm with a thickness of 4 mm) from which the failure stress was obtained. The first sample group exhibited a waveguide and WBG in the center of the glass (configuration see Figure S14 in Supporting Information) inscribed with the optimal laser parameters (waveguide: pulse energy 350 nJ, writing speed 0.5 mm/s; WBG: pulse energy 250 nJ, speed 0.5 mm/s, duty cycle 50%; writing depth 100 μm), and the second group, serving as a reference, consisted of unmodified glass. The orientation of the WBG was chosen perpendicular to the bending direction (longitudinal direction) representing the most severe and potentially the worst-case scenario for impacting the glass strength. Before analyzing the glass strength based on the failure load, the first step is to determine the failure location to verify the validity of the test. Since the failure location identifies the weakest spot of the glass, it must be within the loading span in which the stress is maximum and uniform [51]. The results showed that all sixty samples failed within the acceptable span, originating either from the surface or the edge (cfr. Figure S9 in Supporting Information).

A two-parameter Weibull distribution [52] was applied to analyze the experimental data collected from these specimens. This distribution, commonly used to model the strength of glass, effectively describes the probability of failure [21a, 53]. Figure 3b displays the Weibull distribution for the tested specimens including photos showing examples of edge and surface failures in both WBG and reference samples. The results showed that the mean strength of the samples with WBG was 68.8 ± 10.6 MPa (n=30), while the mean strength for the reference (non-WBG) samples was 79.6 ± 17.2 MPa (n=30). Although the glass strength of the reference samples was found marginally higher, failures did not originate from the WBG areas in any of the samples, meaning that their presence did not influence the glass strength. Instead, the observed marginally lower strength can be attributed to potential damage incurred during transportation and additional handling for the re-polishing process, which likely introduced additional surface flaws lowering the glass strength [19, 54]. Notably, only 13.3% of the failures occurred at the edge in the WBG samples, compared to 33.3% in the non-WBG samples. This lower rate of edge failures relative to surface failures further supports the hypothesis that some surface flaws were introduced during handling and transportation, though these flaws were not severe enough to substantially affect the overall strength of the glass. Several key strength parameters are also computed, including the characteristic strength ($\mathrm{P}_{0.05}$), and design strength ($\mathrm{P}_{0.008}$), which are detailed in Table S1 in the Supporting Information. These observations lead to the conclusion that the WBG does not compromise the structural integrity of the glass, as evidenced by the absence of failures originating from the WBG areas.

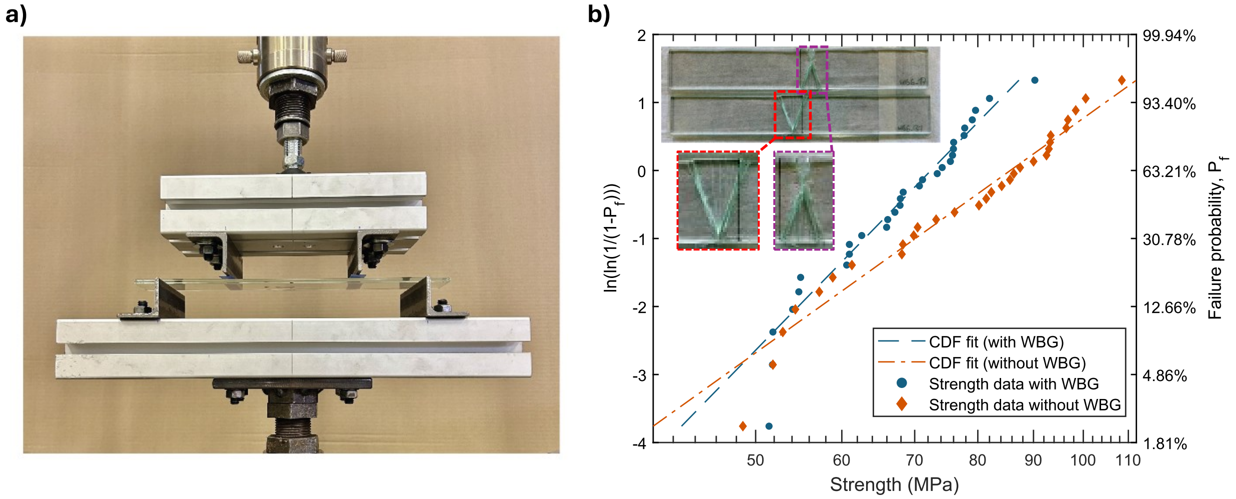

Figure 3. a) Four-point bending test setup used for strength and functional verification tests. b) Weibull distribution of glass samples with (n=30) and without WBG (non-WBG, n=30) with cumulative distribution function (CDF) fits; inset photos: examples of edge (bottom left photo) and surface (bottom right photo) failures.

2.4. Functional demonstration of Bragg grating-based sensing in architectural glass

As a proof-of-concept demonstration towards monitoring architectural glass and to evaluate the sensor's sensitivity to strain and temperature, a functional WBG sensor was integrated in the center of a glass sample measuring 250 × 38.1 ± 3.2 mm with a nominal thickness of 4 mm. This sample was sufficiently large for reliable mechanical characterization and with the help of a single mode fiber connected at the edge, the Bragg grating sensor response was monitored in situ.

2.4.1. Strain sensitivity

Figure 4a depicts the demonstrator specimen with the WBG centrally located and a strain gauge positioned directly above it as a reference sensor, while Figure 4b shows a schematic side view of the demonstrator, highlighting how the fiber is attached to the sample using adhesive and a supporting glass piece securing the attachment. The same 4-point bending setup used for the strength tests, as shown in Figure 3a, was employed to apply a bending load resulting in a uniformly strained glass region between the inner loading span. During loading, readings were taken at 13 intervals for positive strain and 11 intervals for negative strain and the shift in Bragg wavelength was plotted against the strain measured by the reference strain gauge. The maximum stress applied during this experiment was determined to be as close as possible to the sample's maximum tolerable stress without causing failure. The strain response of the WBG, illustrated in Figure 4c, indicates a sensitivity of 1.20 pm/με. It is important to note that to extract the WBG sensitivity, a compensation was performed taking into account the slightly lower strain experienced at a depth of 100 μm below the surface (WBG location) compared to the strain at the surface (reference strain gage), assuming a linear strain distribution through the glass thickness, as illustrated in Figure S5 (Supporting Information). Although specific values for the strain sensitivity of SLS glass are not available from literature, the obtained sensitivity is comparable to laser-written Bragg gratings in fused silica, with reported sensitivities ranging from 1.10 pm/με [55] to 1.23 pm/με [10b, 56]. In comparison, the strain sensitivity of FBGs range from 1.22 pm/με for silica fiber to 2.76 pm/με for β-ZnS (CVD) fiber [57].

The relative sensor sensitivity to strain can be expressed as $\Delta\lambda/\lambda_{B,0} = (1 - p_e)\Delta\varepsilon$ [58], where $\lambda_{B,0}$ is the Bragg wavelength at the reference state and p_e is the effective strain-optic coefficient. For the given Bragg wavelength, $\lambda_{B,0}$ = 1533 nm, the effective strain-optic coefficient (p_e) for the used architectural SLS glass is calculated to be 0.22 ppm/με. This value matches the reported value of 0.22 ppm/με for silica FBGs [58-59].

2.4.2. Temperature sensitivity

To assess the sensitivity of the WBG to temperature, the demonstrator was placed in an environmental chamber set to temperatures ranging from approximately 10°C to 70°C while the actual temperature was measured more precisely using a thermocouple attached just next to the WBG sensor. Figure 4d plots the Bragg wavelength shift of the WBG (average of 6 measurements at each temperature interval) as a function of the reference temperature showing a temperature sensitivity of 13.5 pm/°C. This value for SLS glass is comparable to sensitivities of Bragg gratings written in planar fused silica glass, having reported values ranging from 10 pm/°C to 13.7 pm/°C [10b, 45, 55, 60]. FBGs in chalcogenide fibers exhibit higher temperature sensitivity, with As_2S_3 fiber showing the highest sensitivity coefficient of 175.7 pm/°C, compared to silica fibers, which have the lowest at 11.3 pm/°C [57].

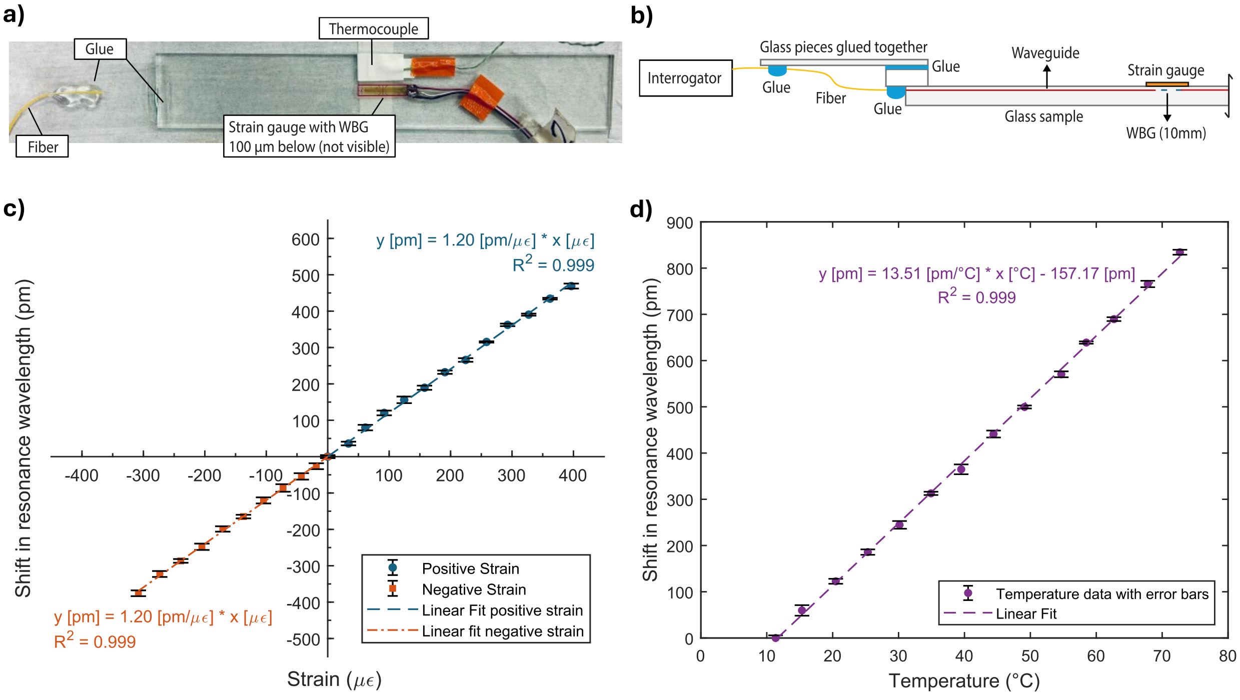

Figure 4. a) Top view of the demonstrator specimen showing the WBG centrally located, with a strain gauge positioned directly above it, a thermocouple next to it, and a readout fiber attached at the edge. b) Schematic side view of the

demonstrator specimen illustrating the readout fiber, adhesive, and an auxiliary glass piece configuration. c) Positive and negative strain responses of the WBG. d) Temperature response of the WBG.

The relative sensor sensitivity to temperature can be expressed as $\Delta\lambda/\lambda_{B,0} = (\alpha + \xi)\Delta T$ [61], where α is the coefficient of thermal expansion (CTE) and ξ is the thermo-optic coefficient. Based on the glass composition, the range for the CTE of soda-lime silica glass varies between 7.75 to 15.85 ppm/°C [62]. Accordingly, for the given Bragg wavelength ($\lambda_{B,0}$ = 1533 nm), the thermo-optic coefficient (ξ) is estimated to be in the range of 1.1 to -7 ppm/°C.

Although this type of sensors is stable well beyond the tested temperature range [28c], we limited our testing range due to the fiber coating and glue used for attachment, which would face performance issues at higher temperatures. Additionally, extreme temperature monitoring is generally not required for the targeted SHM applications.

The strain and temperature sensitivity values obtained are comparable to those of standard FBG sensors, which have already demonstrated reliable results for structural monitoring [63]. However, it is known that Bragg grating sensors are sensitive to both strain and temperature and to decouple both influences, various strategies have been reported, depending on the application. For example, when pure bending is expected, a differential sensor could be realized measuring equal magnitudes of strain, but with opposite sign [45]. Assuming both sensors are at the same temperature, they will experience an identical response to temperature so that the differential signal will cancel out temperature influences. Alternatively, a reference temperature sensor could be used, either integrated in the glass [55] or attached as external sensor.

Finally, the applicability and performance of the sensor are largely determined by the quality of the reflection spectrum and the ability to discern the peak at the Bragg wavelength over background reflections and noise. This is limited by coupling loss, waveguide propagation loss, and Bragg grating reflectivity. Although low losses and good Bragg grating reflectivities were achieved, the current distance between the sensor and the interconnecting edge is limited to a few tens of centimeters, as each additional centimeter adds 1 dB of loss (sum of propagation loss in both forward and backward directions). This allows for the implementation of such sensors close to the clamping location, such as in cantilevered beams or clamped panels. However, placing these sensors closer to the center of larger panels would require further reduction in propagation loss and/or an increase in Bragg grating reflectivity. Additionally, implementing sensors in larger glass panels would necessitate more industrial laser systems capable of handling larger sizes and variations.

3. Conclusions

This paper reports on the realization, detailed optimization and characterization of single mode waveguides and waveguide Bragg Grating (WBG) sensors in 4 mm thick architectural SLS glass achieved using femtosecond laser technology aiming at invisible sensors for structural health monitoring of glass without compromising its strength.

Firstly, the optimization of the laser parameters focused on minimizing the propagation loss while keeping the coupling loss to single mode fiber acceptable for operation in the 1550 nm wavelength range. As such, for optimized laser parameters, a propagation loss of 0.52 dB/cm and coupling loss of 1.49 dB was obtained as shown by cut-back measurements. Furthermore, from cross-sectional analysis it was seen that the heat accumulation mechanism caused the local refractive index increase forming the low-loss waveguides. Although an architectural grade (cheaper and assumably lower in quality) SLS glass was used, the achieved low losses are comparable to the lower values reported in literature for higher quality technical grade glass. This finding is significant as it paves the way for the use of femtosecond laser-inscribed structures in architectural glass applications.

Secondly, laser parameters were optimized for achieving WBG sensors with good peak reflectivity of 12.8% (around 1535 nm wavelength) for a 1 cm grating length. A significant impact of the duty cycle on the reflectivity was observed favoring 50 % duty cycle to achieve highest reflectivity.

Thirdly, this study evaluated the structural strength of the 4 mm thick glass containing WBG sensors, with 60 samples tested under four-point bending conditions according to the relevant ASTM standard. The results confirm that the integration of the WBG did not compromise the glass strength, as no failures were associated with the WBG regions.

Finally, a demonstrator featuring a 250 mm long waveguide with central WBG was fabricated and allowed to assess the sensor performance, demonstrating sensitivities of 1.20 pm/με for strain and 13.5 pm/°C for temperature, which is comparable to what has been obtained in technical grade fused silica glass.

This research underscores the potential for incorporating such "invisible" sensors into architectural glass, particularly within the construction industry where SLS glass is prevalent. While practical challenges remain before these sensors can be widely implemented in large-scale applications such as windows, the promising outcomes of this study suggest that the concept is both innovative and feasible. This marks a substantial step toward integrating advanced sensing technology into everyday materials, potentially transforming their use in the construction industry and structural health monitoring.

4. Experimental section

4.1. Materials

The glass used was annealed SLS float glass, with a nominal thickness of 4 mm. Due to its production process, float glass has two distinct sides, one side that was in contact with the tin bath, i.e. the “tin side” and the other side that was in contact with air, i.e. the “air side” [19]. Although no immediate difference in results was observed when inscribing from the tin side or air side, the tin side was chosen for consistency. The tin side was identified from the glow following UV illumination. All subsequent laser fabrication processes were conducted on this identified tin side. The glass composition was analyzed through SEM/EDS analysis, as detailed in Table S2. (Supporting Information). Apart from the estimated composition, the optical transmittance of the SLS glass is measured through UV/VIS spectroscopy, as shown in Figure S10 in Supporting Information. We used architectural glass from a new batch, which was free of flaws. Additionally, we adopted careful handling practices to minimize the appearance of any further flaws or scratches that could interfere with the laser inscription process.

4.2. Laser modification

Waveguides and Bragg gratings were realized using a Satsuma femtosecond laser (Amplitude) equipped with a second harmonic generation module to achieve a lasing wavelength of 515 nm. This laser exhibits a pulse duration of approximately 400 fs and the pulse repetition rate was fixed at 500 kHz. In the beam path, a rotatable half-wave plate and a rotatable quarter-wave plate were integrated, allowing for precise control of the laser light polarization. In the current work, linear polarization aligned parallel to the writing direction was used. The laser beam was focused onto the SLS substrate using an aspheric lens with a numerical aperture (NA) of 0.55 (Newport 5722-A-H). The substrate was secured on a vacuum chuck attached to a motorized XY-stage with sub-micrometer positioning accuracy (cfr. Figure S11 in Supporting Information). Fabrication of the waveguides/gratings involved laterally moving the substrate relative to the laser beam which was incident perpendicularly on the glass. To accurately position the modified regions at the desired depth, the system was equipped with a camera in the beam path which allows precisely locating the glass top surface. The camera provided a live display of the glass surface during irradiation. By moving the objective vertically, the size of the reflected spot captured by the camera changes and the smallest reflected spot indicated that the laser was focused on the glass surface. To ensure uniformity in the writing depth, the waveguide position with respect to the glass surface was checked at both sides of the glass. For realizing the Bragg gratings, an external acousto-optic modulator was used to modulate the 500 kHz pulse train into burst with an adaptable duty cycle [42] (cfr. Figure S12 in Supporting Information). The target Bragg wavelength λ_B was achieved by adjusting the modulation frequency and writing speed to obtain a grating period Λ = 0.510 μm as follows

$$f = \frac{2n_{eff}v}{\lambda_B} \tag{1}$$

$$\Lambda = \frac{v}{f} \tag{2}$$

where f is the external modulation frequency, and v is the writing speed.

4.3. Cross-sectioning, polishing, and microscopic inspection

To allow inspection and optical characterization, optically clear end faces were prepared at the sides of the 4 mm thick glass samples by cutting using a CO_2 laser (power 2.7 W, writing speed 1 mm/s, 6 passes, circular spot size: 600 μm) operating at a wavelength of 9.6 μm. After six passes, the laser inscribed groove rapidly propagated through the entire glass thickness. To avoid damage to the waveguide, this inscription was performed on the other (= air side) side of the glass. Afterwards, the edges of the glass samples were polished using a mechanical cross-section polishing machine (Mecapol P310). The polishing was done sequentially with abrasive papers of different grit sizes: P600 for 5 minutes, P1200 for 5 minutes, and P4000 for 10 minutes, each at a rotation speed of 200 rpm.

An optical microscope (Nikon Eclipse LV100) was used to capture cross-sectional views of the laser modified zones. Diascopic illumination (reflected light mode), combined with polarization settings, was employed to maximize contrast in the modified regions.

4.4. Optical characterization and fiber attachment

The glass samples were mounted on a setup exhibiting 2 motorized XYZ stages to precisely align cleaved input and output single mode fiber (SMF 28) with the previously polished end faces of the waveguide (Bragg grating) sections.

For waveguide loss measurements, the output fiber was connected to a power meter (Newport PM1930, detector Newport 918-IR), while the input fiber was connected to a 1550 nm pigtailed single-mode laser (QPhotonics, model QDFBLD-1550-5). To avoid parasitic Fresnel reflections at the fiber-air and waveguide-air transitions (about 4% for each interface), an index-matching liquid (RI = 1.46 at 589.3 nm, Series A from Cargille) was applied between the optical fiber and the waveguide. A reference measurement was taken by recording the transmitted power when input and output fiber were perfectly aligned without glass sample in between. The waveguide insertion loss was calculated as the ratio of measured transmitted powers without and with the sample positioned between input and output fiber. To measure the near-field mode profiles, a Xenics Xeva infrared camera equipped with a 100x microscope objective was used to image the waveguide output facet while 1550 nm light was coupled in.

For recording the Bragg grating reflection spectra, a circulator (Thorlabs, 6015-3-APC) was used of which port 1 was connected to a superluminescent light emitting diode (SLED) with1550 nm center wavelength and 65 nm 3 dB bandwidth (Exalos EXS1510-1110), port 3 was connected to an Agilent 86142B Optical Spectrum Analyzer (OSA) and port 2 was connected to a cleaved single mode fiber aligned with the sample input end face.

For reading out the sensor responses to strain and temperature on the demonstrator specimen, a more portable FBG-scan 608 interrogator (FOS&S, now FBGS International) was used since these experiments were performed in a separate lab with mechanical testing capabilities. To attach the fiber permanently to the glass sample in preparation for mechanical testing, a UV-curable adhesive (NOA 61, Norland Products) was applied in several steps to prevent alignment issues due to shrinkage. First, a small amount of adhesive was applied to the tip of the fiber, which was then attached to the glass and cured. Next, a larger amount of adhesive was applied around the fiber and cured to cover a larger area where the fiber is attached to the glass. In the subsequent step, an auxiliary glass piece was attached on top of the main sample with adhesive in such a way that it protruded by 4 to 5 cm (cfr. Figure 4b). The purpose of the auxiliary glass piece is to increase the adhesive area and hold the fiber securely during handling and testing. Finally, the sample was removed from the stage, and the coated part of the fiber (3-4 cm from the fiber tip) was glued in one spot to the auxiliary glass piece with the same adhesive to ensure mechanical robustness of the assembly.

4.5. Quasi-static four-point bending tests

4.5.1. Glass strength

Commonly employed testing methods to assess glass strength include four-point bending [51, 64] and co-axial double ring tests [65]. Typically, due to the significant standard deviation in results, a large number of tests (at least 30 samples) are necessary to obtain reliable results in estimating the glass strength [52], which is often influenced by natural flaws occurring during production, transportation, and usage [21b, 66]. Therefore, to determine the effect of WBG on the glass strength, 60 glass samples (air side facing up) were subjected to the four-point bending test according to ASTM C158-02 (2017) [51] (cfr. Figure S13 in Supporting Information) employing a universal testing machine (INSTRON 5982 - 100 kN). 30 samples contained WBG and 30 did not exhibit any laser modification as reference (non-WBG group). The nominal glass dimensions were selected according to the standard and the actual dimensions were measured to be 250 × 38.1 ± 3.2 mm (n = 60) with a nominal thickness of 4 mm. The longitudinal sides of the glass samples were polished to minimize the effect of edge defects. The WBG was realized in the center of the glass along the short direction (worst case scenario) from edge to edge (cfr. Figure S14, Supporting Information). A re-polishing step was followed WBG fabrication to avoid leaving local non-uniform modification on the glass edges. During the four-point bending test, the load was applied at a constant rate of 1.1 ± 0.2 MPa/s and loading continued until failure of the glass specimen [51]. Fractography analysis was then performed to identify the fracture origin, which may occur on either the glass surface or at the edge [21a]. To facilitate this analysis and to secure the glass fragments, a thin adhesive film was attached to the compression face (air side) of the glass specimens just before testing. The negligible compressive stiffness of the tin film did not influence the test results. After the test, the width and thickness of each specimen was measured at the fracture location using a caliper to accurately calculate the real tensile stress.

As mentioned before, due to the brittle nature of glass and the significant variability in its strength caused by natural flaws and defects, the Weibull distribution is essential for understanding the probability of failure under stress and determining an accurate design strength [53b, 67]. Therefore, we employed a two-parameter Weibull distribution using the Weighted Least Squares Regression (WLSR) method [52] to fit the strength data to the Weibull distribution. This method utilizes Bernard's median rank formula to estimate the probabilities corresponding to the observed bending strengths.

4.5.2. Functional demonstration

To evaluate the sensor functionality, a demonstrator glass sample measuring 250 × 38 mm with a nominal thickness of 4 mm and containing a 1 cm-long Bragg grating was prepared. Figure S15 in Supporting Information illustrates the schematic layout of the sample, highlighting the position of the WBG and the waveguides connecting it to the short edges of the glass. The two sides of the sample were polished and a fiber was attached to one side (cfr. above) to facilitate *in situ* sensor readout using an FBG-scan 608 interrogator. A reference strain gauge (PFL-20-11, Tokyo Measuring Instruments Lab) was attached just above the Bragg grating sensor. Additionally, a reference K-type thermocouple was affixed to the glass surface using a thermally conductive adhesive to ensure complete contact, positioned right next to the strain gage (cfr. Figure 4a, Figure S15).

To assess strain sensing capabilities, a universal testing machine (INSTRON 5982 - 100 kN) was used to apply displacement in a stepwise manner (60 μm/step) using the same four-point bending test configuration as used for the glass strength characterization (see Figure S16 in Supporting Information). The displacement steps were selected to ensure the collection of sufficient data before the sample reached failure. Six measurements were taken at each step, the results of which were averaged. Subsequently, the sample was flipped in the setup allowing application of negative strain in a similar manner.

To assess temperature sensitivity, an environmental chamber (INSTRON 3119-607) was employed. The sample was subjected to controlled temperature changes, applied stepwise from approximately 10 °C to 70 °C. At each step, the temperature was allowed to stabilize for 15 minutes, after which six measurements were taken and averaged.

4.6. Statistical Analysis

No data pre-processing was applied in this work unless otherwise mentioned in the manuscript. Wherever relevant, data is presented in the form “mean ± standard deviation” together with the sample size (n). In Figure 2a, a linear fit was obtained using linear regression.

Acknowledgements

The authors wish to thank the Research Foundation - Flanders (FWO) for the financial support on the research project (Grant number G021821N). The authors would also like to thank the lab technicians and support staff for their help.

Conflict of Interest

The authors declare no conflict of interest.

Data Availability Statement

The authors declare that all data supporting the findings of this study are available within the paper and its supplementary information files. Raw data is available from the corresponding author upon reasonable request.

References

[1] a)C. Bedon, X. Zhang, F. Santos, D. Honfi, M. Kozłowski, M. Arrigoni, L. Figuli, D. Lange, *Construction and Building Materials* **2018**, 163, 921; b)M. Vandebroek, C. Louter, R. Caspeele, F. Ensslen, J. Belis, *Engineering structures* **2014**, 79, 96; c)G. Sciacca, E. Katsanos, J. H. Nielsen, *Glass Structures & Engineering* **2022**, 7, 661.
[2] a)W. Lu, Y. Wang, H. Chen, L. Jiang, Q. Duan, M. Li, Q. Wang, J. Sun, *Construction and Building Materials* **2018**, 186, 635; b)G. Campione, S. Benfratello, C. Cucchiara, G. Minafò, *Engineering structures* **2013**, 49, 664; c)F. A. d. Santos, P. F. Gonçalves, C. Cismaşiu, M. Gamboa-Marrufo, *Proceedings of the Institution of Civil Engineers-Structures and Buildings* **2014**, 167, 743.

[3] a)*CEN/TS 19100-1:2021-11: Design of glass structures: Part 1: Basis of design and materials*, CEN, **2021**; b)*CEN/TS 19100-2:2021-11: Design of glass structures: Part 2: Design of out-of-plane loaded glass components* CEN, **2021**; c)*CEN/TS 19100-3:2021-11: Design of glass structures: Part 3: Design of in-plane loaded glass components and their mechanical joints*, CEN, **2021**; d)M. Feldmann, M. Laurs, J. Belis, N. Buljan, A. Criaud, E. Dupont, M. Eliasova, L. Galuppi, P. Hassinen, R. Kasper, *Glass Structures & Engineering* **2023**, 8, 317.

[4] a)A. Moreno-Gomez, C. A. Perez-Ramirez, A. Dominguez-Gonzalez, M. Valtierra-Rodriguez, O. Chavez-Alegria, J. P. Amezquita-Sanchez, *Archives of Computational Methods in Engineering* **2018**, 25, 901; b)C. C. Fu, N. Zhang, *Journal of performance of constructed facilities* **2011**, 25, 309.

[5] H. Sun, A. Mordret, G. A. Prieto, M. N. Toksöz, O. Büyüköztürk, *Mechanical Systems and Signal Processing* **2017**, 85, 468.

[6] T. J. Bajzek, *IEEE Instrumentation & Measurement Magazine* **2005**, 8, 35.

[7] A. Güemes, A. Fernández-López, P. F. Díaz-Maroto, A. Lozano, J. Sierra-Perez, *Sensors* **2018**, 18, 1094.

[8] R. Stoian, *Applied Physics A* **2020**, 126, 438.

[9] a)Y. Nasu, M. Kohtoku, Y. Hibino, *Optics letters* **2005**, 30, 723; b)H. Huang, L.-M. Yang, J. Liu, presented at *Nanophotonics and Macrophotonics for Space Environments V*, **2011**.

[10] a)D. Grobnic, S. J. Mihailov, C. W. Smelser, R. Walker, presented at *Photonics North 2007*, **2007**; b)H. Zhang, S. Ho, S. M. Eaton, J. Li, P. R. Herman, *Optics express* **2008**, 16, 14015; c)V. Maselli, J. R. Grenier, S. Ho, P. R. Herman, *Optics express* **2009**, 17, 11719.

[11] F. Sima, K. Sugioka, R. M. Vázquez, R. Osellame, L. Kelemen, P. Ormos, *Nanophotonics* **2018**, 7, 613.

[12] a)L. Zhong, Y. Wang, D. Tan, J. Qiu, *Laser & Photonics Reviews* **2023**, 17, 2200767; b)X. Han, Y. Wang, J. Hu, L. Zhong, J. Qiu, *Laser & Photonics Reviews*, n/a, 2400060.

[13] a)A. Saliminia, N. Nguyen, M.-C. Nadeau, S. Petit, S. Chin, R. Vallée, *Journal of Applied Physics* **2003**, 93, 3724; b)V. Bhardwaj, P. Corkum, D. Rayner, C. Hnatovsky, E. Simova, R. Taylor, *Optics letters* **2004**, 29, 1312; c)V. A. Amorim, J. M. Maia, D. Viveiros, P. Marques, *Journal of Lightwave Technology* **2019**, 37, 2240.

[14] a)K. Mittholiya, P. Anshad, A. Mallik, S. Bhardwaj, A. Hegde, A. Bhatnagar, R. Bernard, J. Dharmadhikari, D. Mathur, A. Dharmadhikari, *Journal of Optics* **2017**, 46, 304; b)L. Sansoni, F. Sciarrino, G. Vallone, P. Mataloni, A. Crespi, R. Ramponi, R. Osellame, *Physical review letters* **2010**, 105, 200503.

[15] a)J. W. Chan, T. R. Huser, S. H. Risbud, J. S. Hayden, D. M. Krol, *Applied physics letters* **2003**, 82, 2371; b)L. B. Fletcher, J. J. Witcher, N. Troy, S. T. Reis, R. K. Brow, D. M. Krol, *Optics express* **2011**, 19, 7929.

[16] M. Hughes, W. Yang, D. Hewak, *Applied Physics Letters* **2007**, 90.

[17] a)K. M. Davis, K. Miura, N. Sugimoto, K. Hirao, *Optics letters* **1996**, 21, 1729; b)F. Chen, J. V. de Aldana, *Laser & Photonics Reviews* **2014**, 8, 251.

[18] a)A. Kowalevicz, V. Sharma, E. Ippen, J. G. Fujimoto, K. Minoshima, *Optics letters* **2005**, 30, 1060; b)L. Tong, R. R. Gattass, I. Maxwell, J. B. Ashcom, E. Mazur, *Optics communications* **2006**, 259, 626; c)I. Dyakonov, A. Kalinkin, M. Y. Saygin, A. Abroskin, I. Radchenko, S. Straupe, S. Kulik, *Applied Physics B* **2016**, 122, 1.

[19] J. Belis, C. Louter, J. H. Nielsen, J. Schneider, in *Springer handbook of glass*, Springer, 2019.

[20] M. Haldimann, A. Luible, M. Overend, *Structural use of glass*, Vol. 10, Iabse, **2008**.

[21] a)S. Nategh, J. Missinne, P. Vijverman, G. Van Steenberge, J. Belis, *Construction and Building Materials* **2021**, 295, 123590; b)N. Bensaid, S. Benbahouche, F. Roumili, J.-C. Sangleboeuf, J.-B. Le Cam, T. Rouxel, *Journal of Non-Crystalline Solids* **2018**, 483, 65; c)T. Rouxel, J.-i. Jang, U.

Ramamurty, *Progress in Materials Science* **2021**, 121, 100834; d)J. Gong, Y. Chen, C. Li, *Journal of non-crystalline solids* **2001**, 279, 219.
[22] J.-S. Boisvert, S. Loranger, P. Lorre, V. L. Iezzi, R. Kashyap, *Journal of Non-Crystalline Solids* **2019**, 521, 119467.
[23] A. Griffiths, *Philosofical Transaction of the Royal Society* **1921**, 221, 163.
[24] T. Erdogan, *Journal of lightwave technology* **1997**, 15, 1277.
[25] A. D. Kersey, M. A. Davis, H. J. Patrick, M. LeBlanc, K. P. Koo, C. G. Askins, M. A. Putnam, E. J. Friebele, *Journal of lightwave technology* **1997**, 15, 1442.
[26] a)M. Thiel, G. Flachenecker, W. Schade, *Optics Letters* **2015**, 40, 1266; b)G. D. Marshall, M. Ams, M. J. Withford, *Optics Letters* **2006**, 31, 2690; c)M. A. Butt, N. L. Kazanskiy, S. N. Khonina, *Biosensors* **2022**, 12, 497.
[27] a)I. Miyamoto, K. Cvecek, M. Schmidt, *Optics Express* **2011**, 19, 10714; b)I. Miyamoto, Y. Okamoto, R. Tanabe, Y. Ito, K. Cvecek, M. Schmidt, *Optics Express* **2016**, 24, 25718.
[28] a)C. B. Schaffer, J. F. García, E. Mazur, *Applied Physics A* **2003**, 76, 351; b)S. M. Eaton, H. Zhang, P. R. Herman, F. Yoshino, L. Shah, J. Bovatsek, A. Y. Arai, *Optics express* **2005**, 13, 4708; c)S. M. Eaton, H. Zhang, M. L. Ng, J. Li, W.-J. Chen, S. Ho, P. R. Herman, *Optics express* **2008**, 16, 9443.
[29] S. M. Eaton, M. L. Ng, J. Bonse, A. Mermillod-Blondin, H. Zhang, A. Rosenfeld, P. R. Herman, *Applied optics* **2008**, 47, 2098.
[30] X. Li, F. Liu, R. Wan, W. Li, P. Wang, *Optics & Laser Technology* **2023**, 161, 109216.
[31] a)S. Piacentini, T. Vogl, G. Corrielli, P. K. Lam, R. Osellame, *Laser & Photonics Reviews* **2021**, 15, 2000167; b)Y.-D. Wang, Z.-Z. Li, Y.-C. Li, Y.-Z. Duan, L.-C. Wang, Y.-H. Yu, Q.-D. Chen, *Optics Letters* **2023**, 48, 554.
[32] a)B. Poumellec, L. Sudrie, M. Franco, B. Prade, A. Mysyrowicz, *Optics Express* **2003**, 11, 1070; b)L. A. Fernandes, J. R. Grenier, P. R. Herman, J. S. Aitchison, P. V. Marques, *Optics express* **2012**, 20, 24103.
[33] a)P. Pan, H. Song, Z. Yang, G. Ren, J. Xiao, X. Chen, J. Xu, *Silicon* **2021**, 13, 3163; b)A. Malewski, M. Kozłowski, J. Podwórny, M. Środa, W. Sumelka, *Materials* **2023**, 16, 397; c)U. Akkasoglu, S. Sengul, I. Arslan, B. Ozturk, B. Cicek, *Journal of Materials Science: Materials in Electronics* **2021**, 32, 22629.
[34] C. Hnatovsky, R. Taylor, E. Simova, P. Rajeev, D. Rayner, V. Bhardwaj, P. Corkum, *Applied Physics A* **2006**, 84, 47.
[35] a)C. Chen, Z. Yang, T. Wang, Y. Wang, K. Gao, J. Wu, J. Wang, J. Qiu, D. Tan, *Nature Communications* **2024**, 15, 9047; b)Z. Li, Y. Wang, J. Wu, Z. Wang, M. Lou, K. Sun, J. Qiu, D. Tan, *Optics and Lasers in Engineering* **2024**, 182, 108467.
[36] a)M. Zaccaria, M. Dubru, N. Lucca, A. Šikyňová, *ce/papers* **2021**, 4, 135; b)M. Toliopoulou, J. O'Callaghan, P. de Ruiter, presented at *Challenging Glass Conference Proceedings*, **2024**.
[37] a)J. Lapointe, M. Gagné, M.-J. Li, R. Kashyap, *Optics express* **2014**, 22, 15473; b)M. Ams, P. Dekker, S. Gross, M. J. Withford, *Nanophotonics* **2017**, 6, 743.
[38] A. Shehata, M. Ali, R. Schuch, T. Mohamed, *Optics & Laser Technology* **2019**, 116, 276.
[39] S. M. Eaton, W.-J. Chen, H. Zhang, R. Iyer, J. Li, M. L. Ng, S. Ho, J. S. Aitchison, P. R. Herman, *Journal of Lightwave Technology* **2009**, 27, 1079.
[40] a)D. Liu, Y. Li, R. An, Y. Dou, H. Yang, Q. Gong, *Applied Physics A* **2006**, 84, 257; b)J.-P. Bérubé, R. Vallée, *Optics letters* **2016**, 41, 3074.
[41] a)G. Carturan, N. Khandelwal, L. Tognana, V. M. Sglavo, *Journal of non-crystalline solids* **2007**, 353, 1540; b)P. Bandyopadhyay, A. Dey, S. Roy, A. K. Mukhopadhyay, *Journal of non-crystalline solids* **2012**, 358, 1091.
[42] H. Zhang, S. M. Eaton, P. R. Herman, *Optics letters* **2007**, 32, 2559.

[43] C. Miese, M. J. Withford, A. Fuerbach, *Optics express* **2011**, 19, 19542.

[44] J. He, B. Xu, X. Xu, C. Liao, Y. Wang, *Photonic Sensors* **2021**, 11, 203.

[45] V. Geudens, G. Van Steenberge, J. Missinne, *IEEE Sensors Journal* **2024**.

[46] S. P. Ugale, V. Mishra, presented at *2011 International Conference on Communications and Signal Processing*, **2011**.

[47] C. Ghosh, Q. M. Alfred, B. Ghosh, *Int. J. Innov. Res. Comput. Commun. Eng* **2015**, 3, 456.

[48] H. Zhang, S. M. Eaton, J. Li, P. R. Herman, *Optics letters* **2006**, 31, 3495.

[49] D. Kang, S. Park, C. Hong, C.-G. Kim, *NDT & E International* **2005**, 38, 712.

[50] S. Nategh, M. Zaccaria, J. Missinne, J. Belis, *Glass Structures & Engineering* **2022**, 7, 471.

[51] *ASTM C158-02, Standard Test Methods for Strength of Glass by Flexure (Determination of Modulus of Rupture), ASTM International, West Conshohocken, PA*, ASTM International, **2017**.

[52] K. C. Datsiou, M. Overend, *Structural Safety* **2018**, 73, 29.

[53] a)M. Vandebroek, J. Belis, C. Louter, G. Van Tendeloo, *Engineering Fracture Mechanics* **2012**, 96, 480; b)M. Zaccaria, M. Overend, *Journal of Materials in Civil Engineering* **2016**, 28, 04015127.

[54] A. K. Varshneya, *International Journal of Applied Glass Science* **2018**, 9, 140.

[55] V. Geudens, S. Nategh, G. Van Steenberge, J. Belis, J. Missinne, *Optics & Laser Technology* **2024**, 169, 109970.

[56] C. E. Campanella, A. Cuccovillo, C. Campanella, A. Yurt, V. M. Passaro, *Sensors* **2018**, 18, 3115.

[57] W. Gao, X. Li, P. Wang, L. Chen, C. Ni, L. Chen, X. Chen, Y. Zhou, W. Zhang, J. Hu, *Optik* **2018**, 156, 13.

[58] G. Hegde, S. Asokan, G. Hegde, *ISSS Journal of Micro and Smart Systems* **2022**, 11, 257.

[59] M. Mansoursamaei, A. Malakzadeh, *Optical Review* **2021**, 28, 289.

[60] C. V. N. Bhaskar, S. Pal, P. K. Pattnaik, *Results in Optics* **2021**, 5, 100130.

[61] Q. Yu, Y. Zhang, Y. Dong, Y. P. Li, C. Wang, H. Chen, presented at *2012 Symposium on Photonics and Optoelectronics*, **2012**.

[62] a)*EN 572-1:2012+A1:2016 Glass in building – Basic soda lime silicate glass products – Part 1: Definitions and general physical and mechanical properties*, European Committee for Standardization, **2016**; b)G. Ghosh, *Handbook of optical constants of solids: Chapter 3 - Thermo-Optic Coefficients*, Academic Press, **1998**; c)J. M. Jewell, *Journal of non-crystalline solids* **1992**, 146, 145.

[63] D. Kinet, P. Mégret, K. W. Goossen, L. Qiu, D. Heider, C. Caucheteur, *Sensors* **2014**, 14, 7394.

[64] *EN 1288-3, Glass in building - Determination of the bending strength of glass - Part 3: Test with specimen supported at two points (four point bending)*, European Committee for Standardization, **2016**.

[65] a)*EN 1288-2, Glass in building - Determination of bending strength of glass - Part 2: Coaxial double ring test on flat specimens with large test surface areas*, European Committee for Standardization, **2016**; b)*EN 1288-5, Glass in building - Determination of the bending strength of glass - Part 5: Coaxial double ring test on flat specimens with small test surface areas*, European Committee for Standardization, **2016**; c)*ASTM, C1499–19, Standard Test Method for Monotonic Equibiaxial Flexural Strength of Advanced Ceramics at Ambient Temperature, ASTM International, West Conshohocken, PA*, ASTM International, **2019**.

[66] a)E. B. Shand, *Journal of the American Ceramic Society* **1961**, 44, 451; b)D. Kinsella, E. Serrano, *Glass Structures & Engineering* **2021**, 6, 397.

[67] a)R. A. Behr, M. Karson, J. E. Minor, *Structural safety* **1991**, 11, 43; b)S. Schula, J. Schneider, M. Vandebroek, J. Belis, presented at *COST Action TU0905 Mid-term Conference on Structural Glass*, **2013**.

Supporting Information

Femtosecond Laser-Written Invisible Sensors in Architectural Glass and their Impact on Strength

Shahryar Nategh [a,b], Viktor Geudens [a], Geert Van Steenberge [a], Jan Belis [b,+], Jeroen Missinne [a,+,*]

[a] Centre for Microsystems Technology (CMST), imec and Ghent University, Technologiepark-Zwijnaarde 126, 9052, Belgium

[b] Magnel-Vandepitte Laboratory, Department of Structural Engineering and Building Materials, Ghent University, Technologiepark-Zwijnaarde 60, 9052, Belgium

[+] Contributed equally as last author

[*] Corresponding author, Jeroen.Missinne@UGent.be

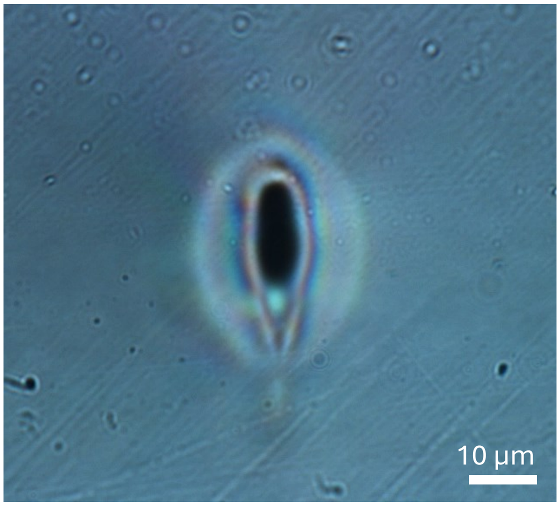

Figure S1. Cross-section of a laser-written line (laser parameters: 0.5 mm/s, 350 nJ, 500 kHz, depth 100 µm) in SLS glass supporting light propagation and visualized using optical transmission microscopy.

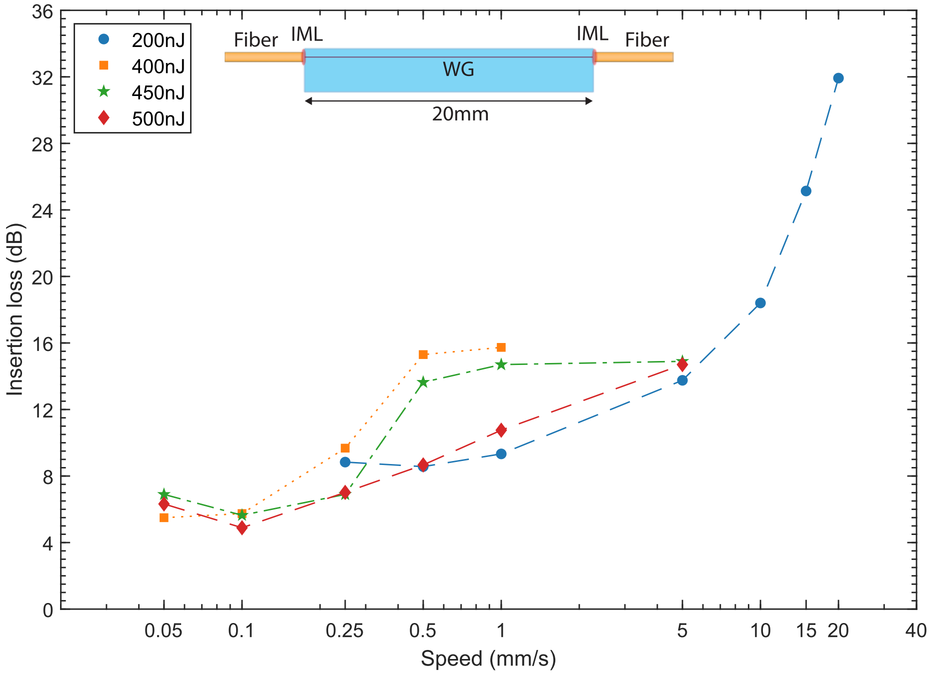

Figure S2. Total insertion loss for 20 mm long waveguides (WG) written at a depth of 100 µm in architectural SLS glass, with varying pulse energies and writing speeds. The schematic illustrates the loss measurement configuration, including the glass WG sample, single mode fibers, and index matching liquid (IML).

Figure S3. (Middle) Microscopic cross-section using episcopic illumination, for waveguides written with a pulse energy of 600 nJ and a speed of 0.05 mm/s. (Left and right) The corresponding near-field profiles revealing two guiding regions: one towards the left side and one towards the right side of the laser modified zone.

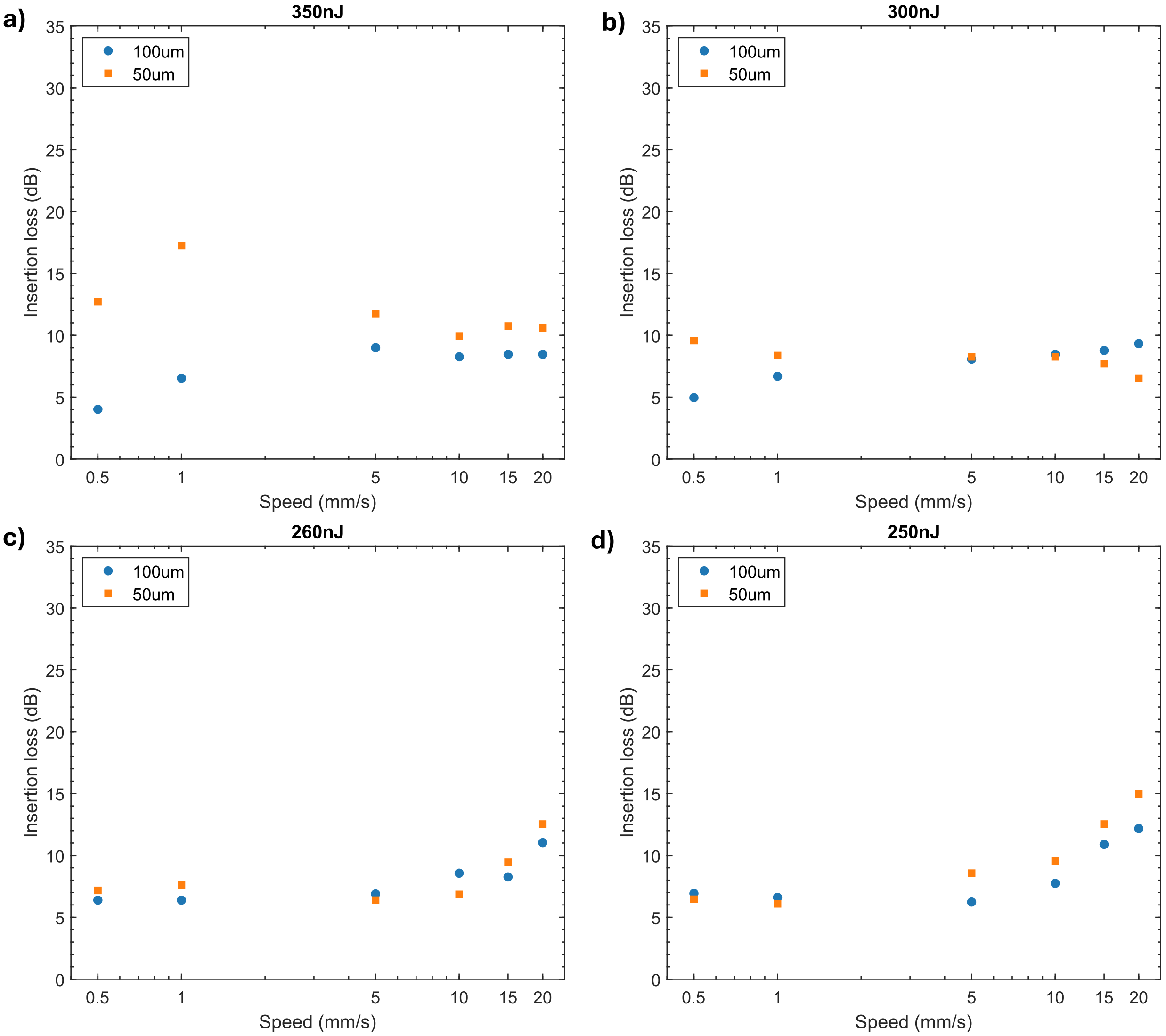
a)
350nJ
b)
300nJ
c)
260nJ
d)
250nJ
100um
50um
Insertion loss (dB)
0
5
10
15
20
25
30
35
Speed (mm/s)
0.5
1
5
10
15
20

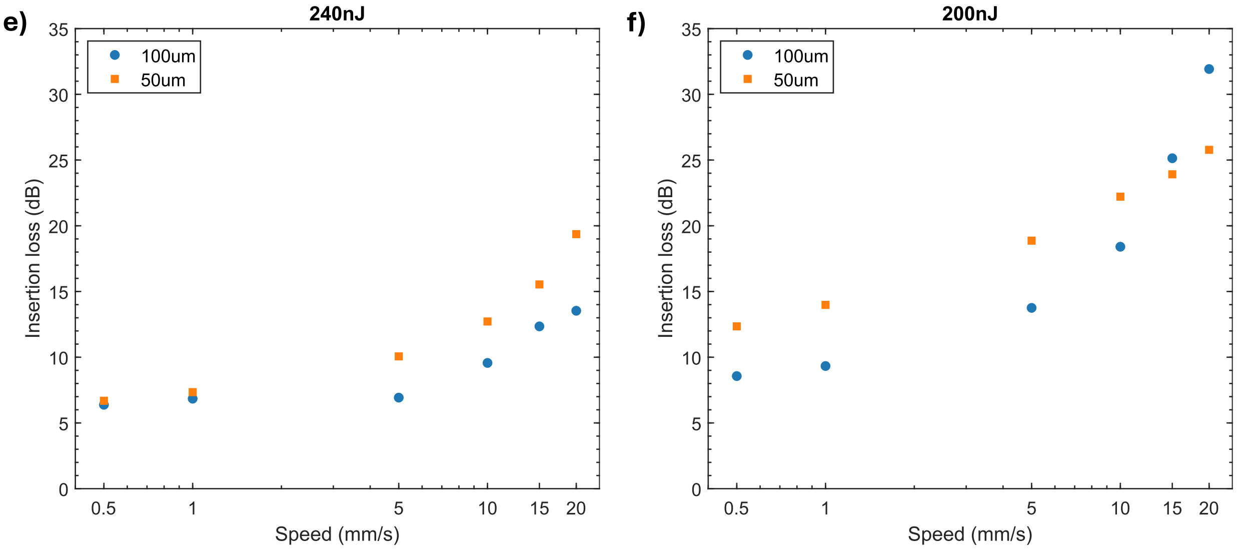

Figure S4. Comparing insertion loss for 20 mm long waveguides fabricated at depths of 100 µm and 50 µm, for laser pulse energies of a) 350 nJ, b) 300 nJ, c) 260 nJ, d) 250 nJ, e) 240 nJ, and f) 200 nJ evaluated with varying writing speeds.

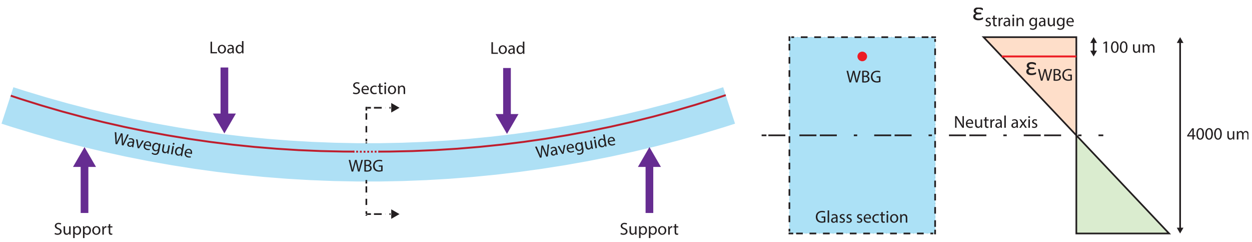

Figure S5. Left: Schematic of the glass cross-section (aspect ratio adjusted for better visibility) showing the WBG location. Right: Strain profile through the thickness of a 4 mm thick glass piece undergoing bending illustrating that a strain gage attached to the surface will undergo a slightly larger strain compared to the waveguide Bragg grating sensor located 100 µm below the surface.

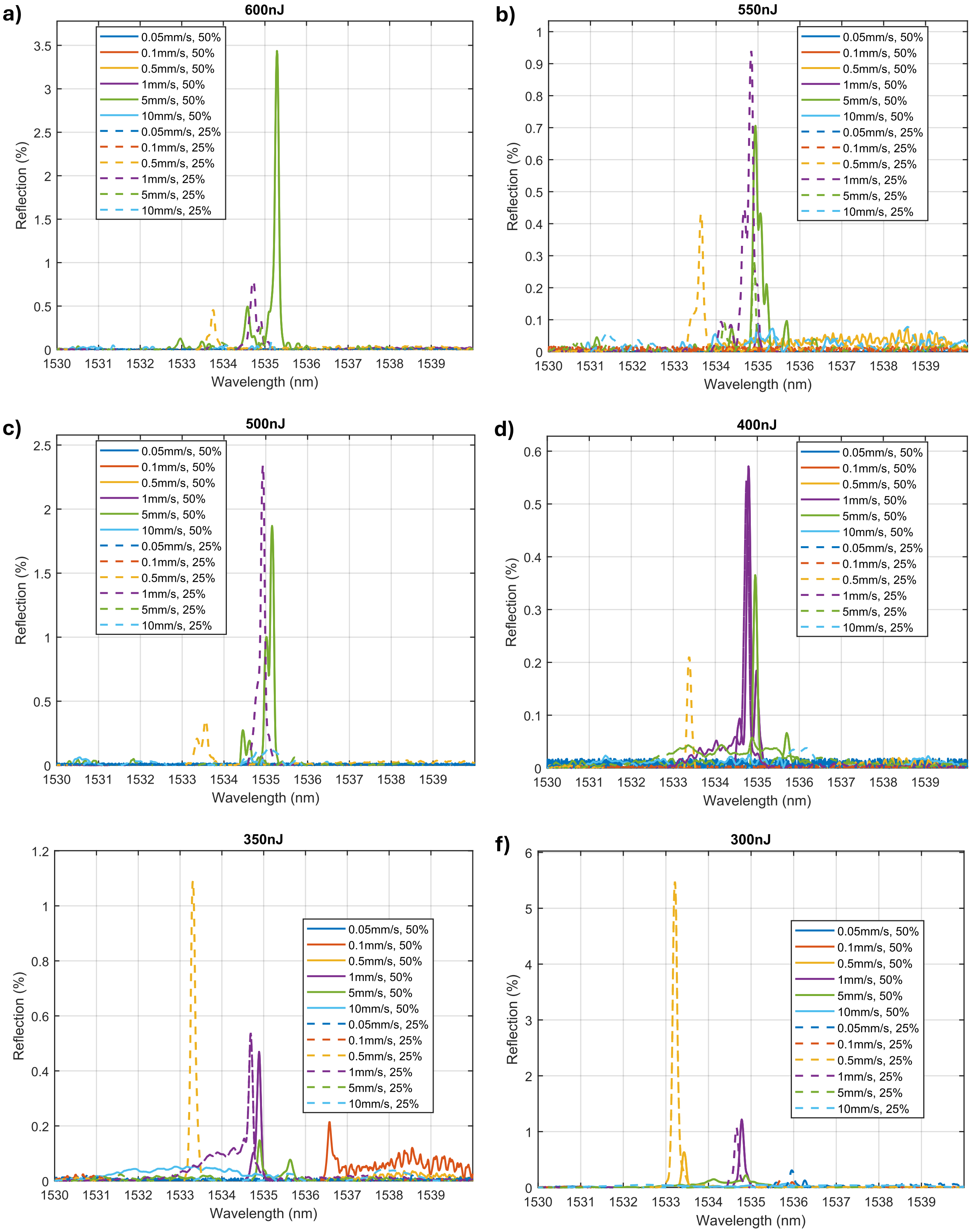
a)
600nJ
Reflection (%)
0
0.5
1
1.5
2
2.5
3
3.5
Wavelength (nm)
1530
1531
1532
1533
1534
1535
1536
1537
1538
1539
0.05mm/s, 50%
0.1mm/s, 50%
0.5mm/s, 50%
1mm/s, 50%
5mm/s, 50%
10mm/s, 50%
0.05mm/s, 25%
0.1mm/s, 25%
0.5mm/s, 25%
1mm/s, 25%
5mm/s, 25%
10mm/s, 25%
b)
550nJ
Reflection (%)
0
0.1
0.2
0.3
0.4
0.5
0.6
0.7
0.8
0.9
1
Wavelength (nm)
1530
1531
1532
1533
1534
1535
1536
1537
1538
1539
0.05mm/s, 50%
0.1mm/s, 50%
0.5mm/s, 50%
1mm/s, 50%
5mm/s, 50%
10mm/s, 50%
0.05mm/s, 25%
0.1mm/s, 25%
0.5mm/s, 25%
1mm/s, 25%
5mm/s, 25%
10mm/s, 25%
c)
500nJ
Reflection (%)
0
0.5
1
1.5
2
2.5
Wavelength (nm)
1530
1531
1532
1533
1534
1535
1536
1537
1538
1539
0.05mm/s, 50%
0.1mm/s, 50%
0.5mm/s, 50%
1mm/s, 50%
5mm/s, 50%
10mm/s, 50%
0.05mm/s, 25%
0.1mm/s, 25%
0.5mm/s, 25%
1mm/s, 25%
5mm/s, 25%
10mm/s, 25%
d)
400nJ
Reflection (%)
0
0.1
0.2
0.3
0.4
0.5
0.6
Wavelength (nm)
1530
1531
1532
1533
1534
1535
1536
1537
1538
1539
0.05mm/s, 50%
0.1mm/s, 50%
0.5mm/s, 50%
1mm/s, 50%
5mm/s, 50%
10mm/s, 50%
0.05mm/s, 25%
0.1mm/s, 25%
0.5mm/s, 25%
1mm/s, 25%
5mm/s, 25%
10mm/s, 25%
350nJ
Reflection (%)
0
0.2
0.4
0.6
0.8
1
1.2
Wavelength (nm)
1530
1531
1532
1533
1534
1535
1536
1537
1538
1539
0.05mm/s, 50%
0.1mm/s, 50%
0.5mm/s, 50%
1mm/s, 50%
5mm/s, 50%
10mm/s, 50%
0.05mm/s, 25%
0.1mm/s, 25%
0.5mm/s, 25%
1mm/s, 25%
5mm/s, 25%
10mm/s, 25%
f)
300nJ
Reflection (%)
0
1
2
3
4
5
6
Wavelength (nm)
1530
1531
1532
1533
1534
1535
1536
1537
1538
1539
0.05mm/s, 50%
0.1mm/s, 50%
0.5mm/s, 50%
1mm/s, 50%
5mm/s, 50%
10mm/s, 50%
0.05mm/s, 25%
0.1mm/s, 25%
0.5mm/s, 25%
1mm/s, 25%
5mm/s, 25%
10mm/s, 25%

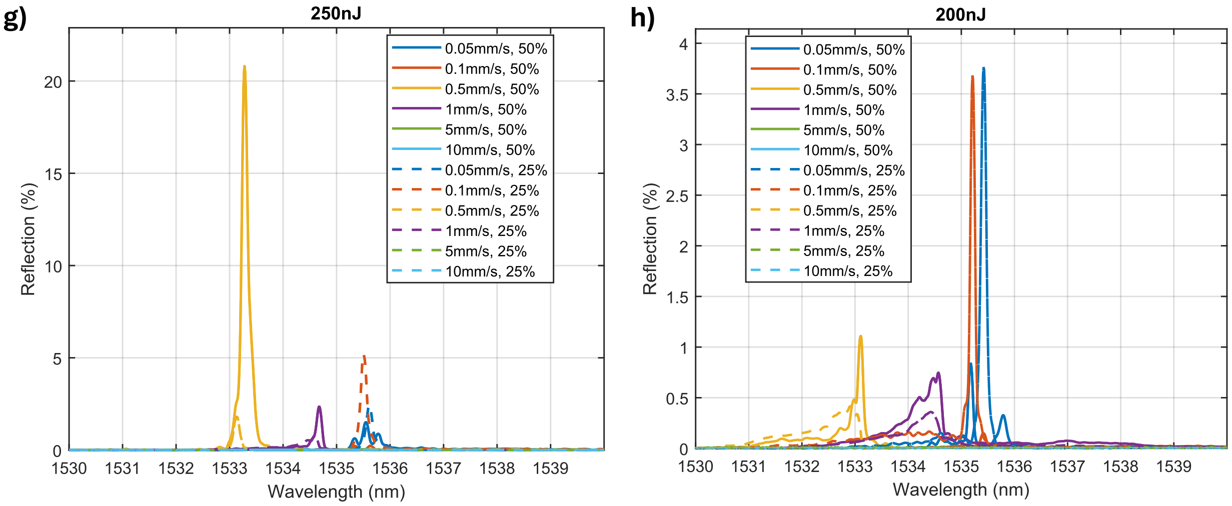

Figure S6. Reflection spectra of 20 mm waveguide Bragg gratings for laser pulse energies of a) 600 nJ, b) 550 nJ, c) 500 nJ, d) 400 nJ, e) 350 nJ, f) 300 nJ, g) 250 nJ, and h) 200 nJ, recorded at various writing speeds and modulation duty cycles. The modulation frequency was calculated using the formula $f = (2n_{eff}\ v)/\lambda_B$, assuming $n_{eff} = 1.52$ to obtain $\lambda_B \approx 1550nm$ in all cases.

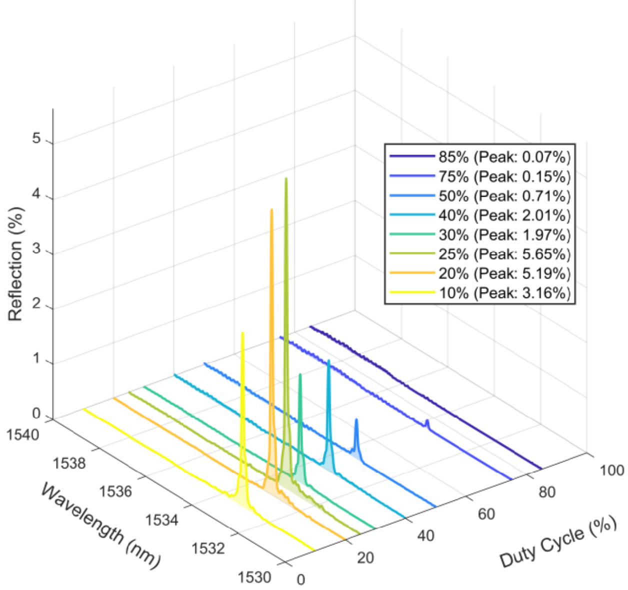

Figure S7. Reflection of 20mm waveguide Bragg gratings for a laser pulse energy of 300 nJ, writing speed of 0.5 mm/s, and different duty cycles.

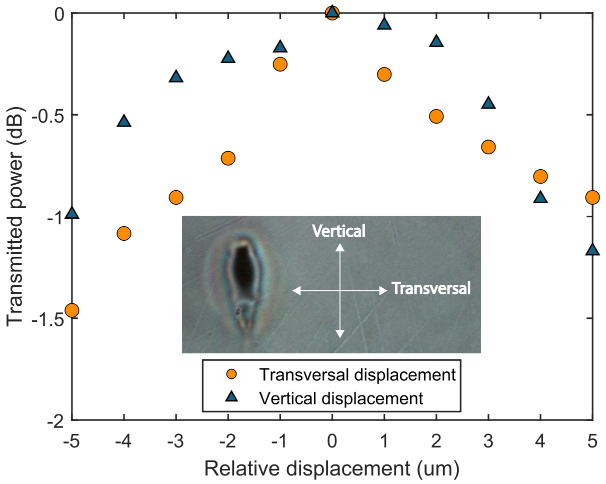

Figure S8. The relative transversal and vertical displacements of the waveguide position with respect to the Bragg gratings position, shown in relation to the transmitted power. The highest transmitted power observed at zero displacement indicates that the laser focus for achieving waveguide and Bragg gratings should be identical with 0 µm transversal offset. The inset image shows the microscopic cross-section of the waveguide written with a pulse energy of 350 nJ and a writing speed of 0.5 mm/s.

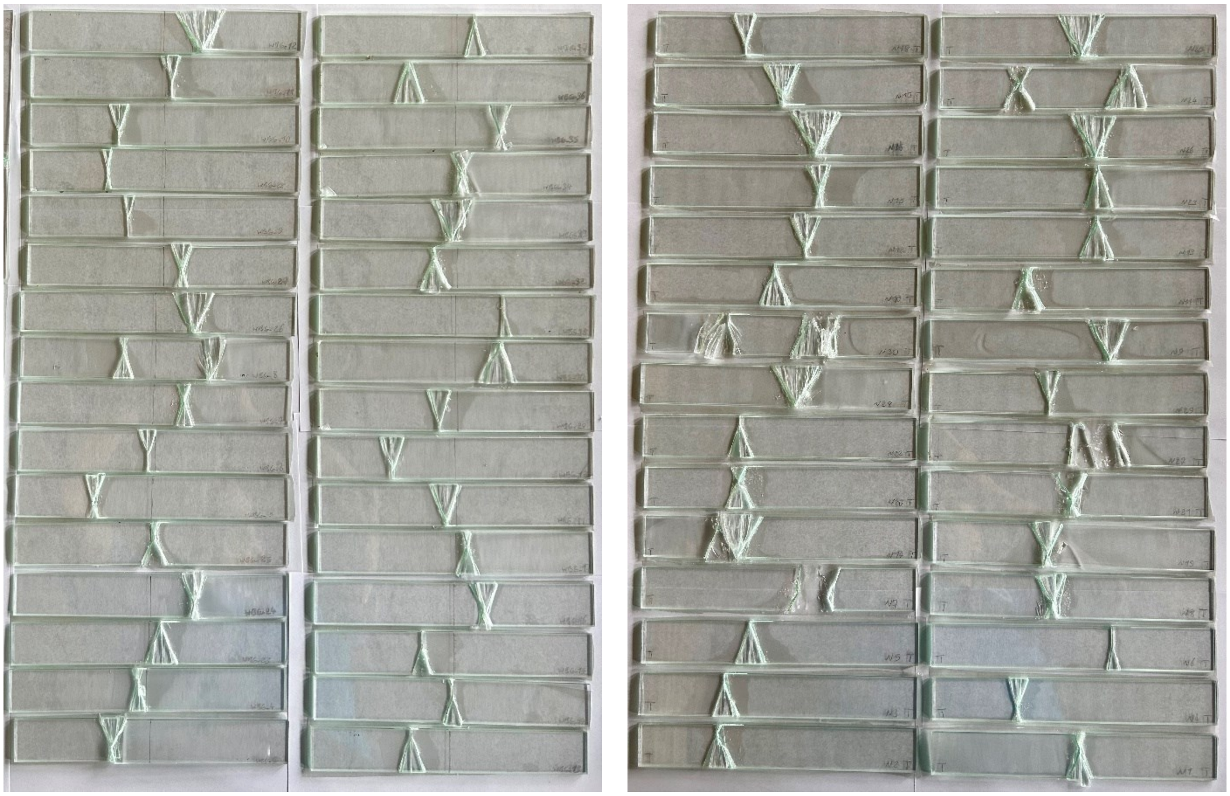

Figure S9. (Left) Fractography of samples with WBG in the center (indicated by the black marker) after four-point bending strength test. Failures occurred at the edges or surfaces. (Right) The reference samples showed similar failure patterns, with some failing at the edges and others at the surfaces.

Table S1. Design, characteristic, and mean strength derived from statistical analysis following the 4-point bending tests of glass specimen with and without inscribed WBG sensors.

	WBG samples	Non-WBG samples
Number of specimens	30	30
Characteristic strength* (MPa)	47.75	47.18
Design strength* (MPa)	36.81	32.50
Mean strength* (MPa)	68.81	79.61
Standard deviation (MPa)	10.59	17.19

* Design strength: failure probability $P_f = 0.008$
* Characteristic strength: failure probability $P_f = 0.05$
* Mean strength: failure probability $P_f = 0.5$

Table S2. Composition of the soda-lime silica (SLS) glass used in this work as obtained using EDS characterization.

Constituents	Proportion by mass of element (%)	
	EDS (current study)	Standard EN 572-1:2012+A1:2016 [94]
Silicon (Si)	34.48	32–35
Calcium (Ca)	9.31	3.5–10.1
Sodium (Na)	8.66	7.4–11.9
Magnesium (Mg)	2.14	0–3.7
Others	-	less than 5

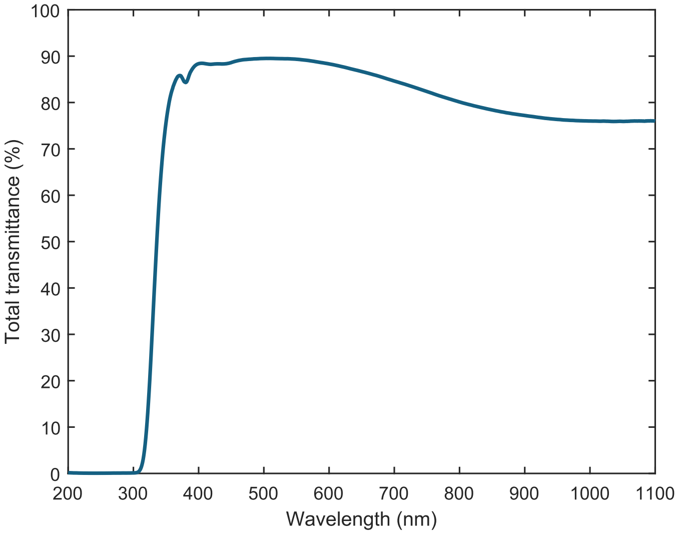

Figure S10. Optical transmittance of the SLS glass (4mm thickness) used in this work

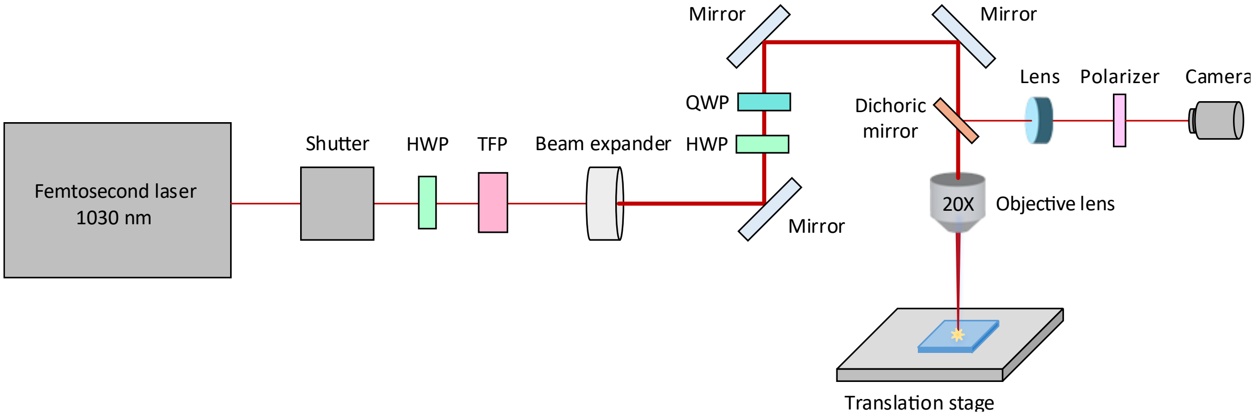

Figure S11. Schematic illustration of the femtosecond laser setup. HWP: Half-Wave Plate, QWP: Quarter-Wave Plate, TFP: Thin-Film Polarizer.

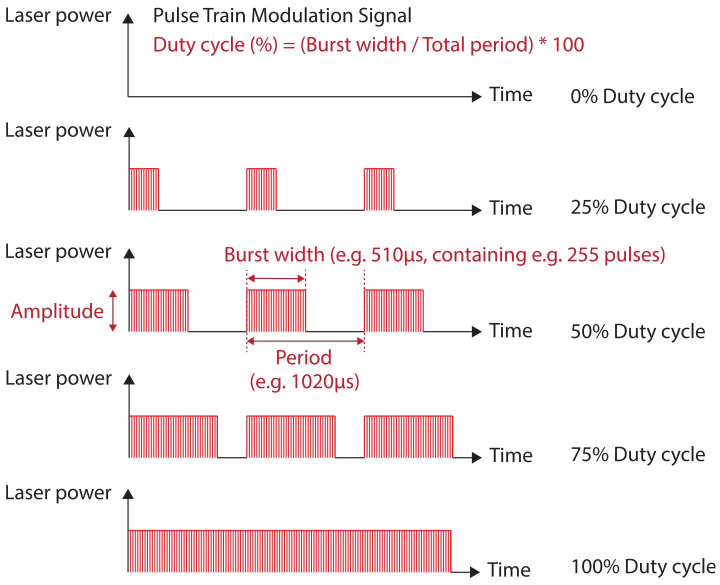

Figure S12. Schematic illustration of the definitions involved for a modulated laser pulse train used in realizing waveguide Bragg gratings (WBG).

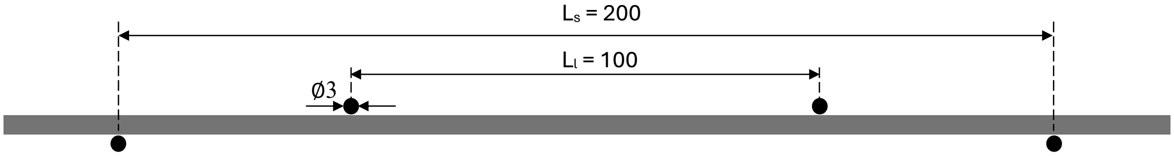

Figure S13. Details of the four-point bending test setup configuration (dimensions in mm).

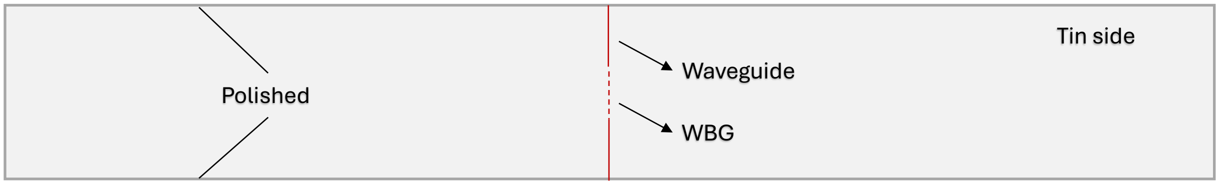

Figure S14. Position of the WG and WBG on the glass specimen for strength tests.

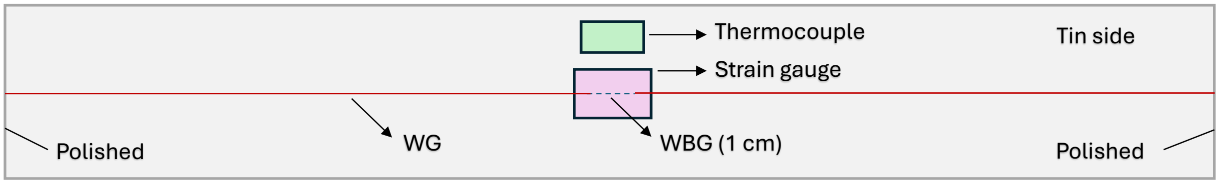

Figure S15. Position of WBG on the glass specimen for verification tests (top view).

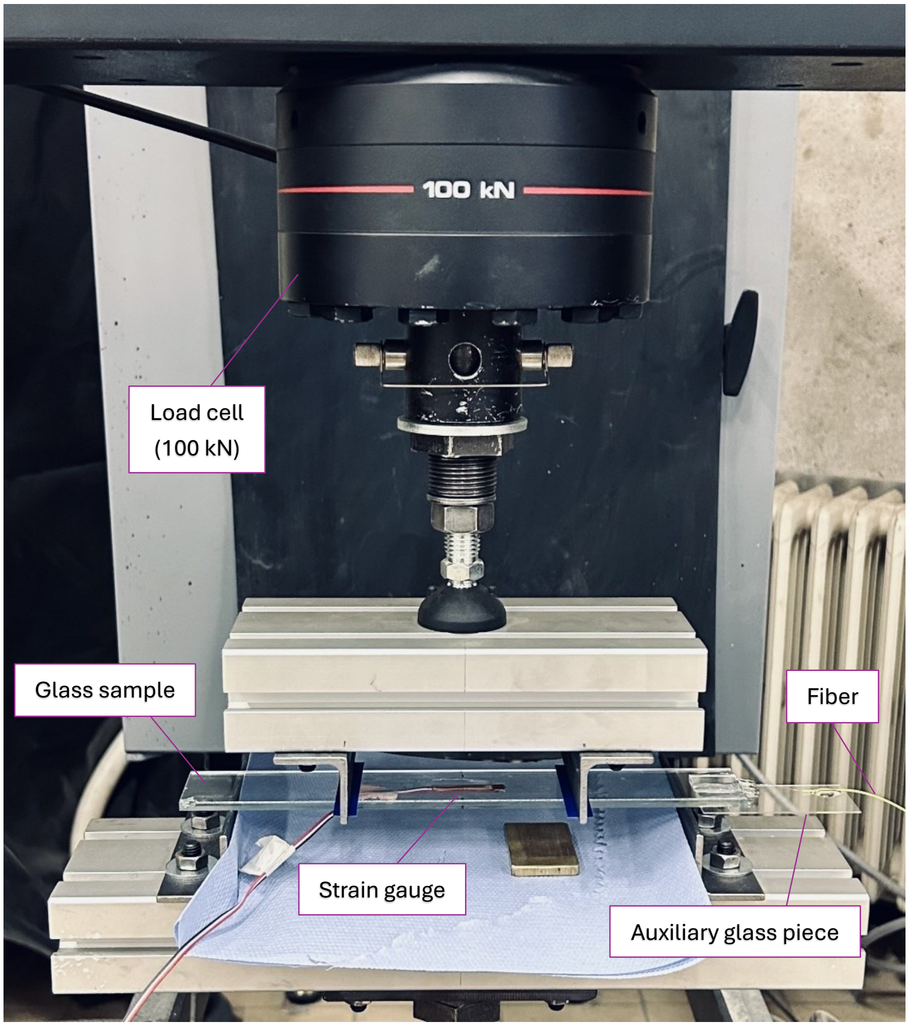

Figure S16. Sample positioned in the four-point bending test setup for functional demonstration test, showing Instron load cell (100 kN), strain gauge, auxiliary glass piece, and fiber.